Florian Loacker-Schöch, BSc

Dynamics Investigation of Buck Converters for Driving High-Power Laser Diodes

Master's Thesis

to achieve the university degree of
Master of Science

Master's degree programme:
Electrical Engineering and Audio Engineering

submitted to

Graz University of Technology

Supervisor
Univ.-Prof. Dipl.-Ing. Dr.techn. Bernd Deutschmann

Institute of Electronics

Graz, January 2021

Affidavit

I declare that I have authored this thesis independently, that I have not used other than the declared sources/resources, and that I have explicitly indicated all material which has been quoted either literally or by content from the sources used.

Date	Signature

Abstract

High-power laser diodes are becoming more and more important in medical applications nowadays and driver efficiency is playing a crucial role in that field. Due to the high power efficiency, the buck converter topology is a promising way forward.
Buck converters for driving high-power laser diodes are investigated in this thesis. Dynamic modeling is performed using the averaged state-space model combined with the two-port network theory. From the modeling results it is shown that a conventional buck converter is not optimal for filtering the output current. Hence, the buck converter was extended with an additional inductance for improving the filter characteristics. Moreover, to compare the modeling with measurements, a 3^{rd} order buck converter based on an integrated gallium nitride (GaN) half-bridge was implemented. Measurements were done on an actual high-power distributed Bragg reflector (DBR) tapered laser diode and the impact of their non-linear load was analyzed. It turns out that the inductance of the load's connecting wires is always present and should be considered. Accordingly, a buck converter 2^{nd} order becomes practical a 3^{rd} order converter. Furthermore, it is confirmed that a 3^{rd} order buck converter is significantly better for filtering the laser current. Finally, the controller design complexity is contrasted with the current filtering characteristics of the 1^{st}, 2^{nd} and 3^{rd} order buck converters.

Kurzfassung

Hochleistungslaserdioden gewinnen heutzutage in medizinischen Anwendungen immer mehr an Bedeutung und die Effizienz der Ansteuerschaltung spielt dabei eine entscheidende Rolle. Aufgrund der hohen Leistungseffizienz ist die Abwärtswandler-Topologie ein vielversprechender Ansatz.
In dieser Arbeit werden Abwärtswandler zur Ansteuerung von Hochleistungslaserdioden untersucht. Die Modellierung der Dynamik wird mit der gemittelten Zustandsraumdarstellung in Kombination mit der Zweitor Netzwerktheorie durchgeführt. Mit den Ergebnissen der Modellierung wird gezeigt, dass ein konventioneller Abwärtswandler nicht optimal für die Filterung des Ausgangsstromes ist. Entsprechend wurde der Abwärtswandler mit einer zusätzlichen Induktivität erweitert, um die Filtereigenschaften zu verbessern. Zum Vergleich der Modellierung mit Messungen wurde zudem ein Abwärtswandler 3. Ordnung basierend auf einer integrierten Galliumnitrid (GaN) Halbbrücke implementiert. Die Messungen wurden dabei an einer realen trapezförmigen Bragg-Spiegel (DBR) Hochleistungslaserdiode durchgeführt und die Auswirkung ihrer nichtlinearen Last analysiert. Es stellt sich heraus, dass die Induktivität der Anschlussdrähte der Last immer vorhanden ist und berücksichtigt werden sollte. Dementsprechend wird aus einem Abwärtswandler 2. Ordnung praktisch ein Wandler 3. Ordnung. Außerdem bestätigt sich, dass ein Abwärtswandler signifikant besser ist, um den Laserstrom zu filtern. Zum Schluss wird die Komplexität des Reglerentwurfes den Filtereigenschaften des Abwärtswandlers 1., 2. und 3. Ordnung gegenübergestellt.

Contents

1. Introduction

Nowadays, lasers are widely used in medical applications and the field is still growing rapidly. Due to the high efficiency and special characteristics of diode lasers system size and cost have been reduced dramatically compared to previous laser technologies. That makes them highly attractive for a wide range of medical applications, such as photo coagulation, dermatology, dentistry and all variations of optical imaging [1].
As a result of higher efficiency at smaller size, laser diode driver circuits have to be adapted to this trend. High laser output power, as frequently desired in medical applications, must be driven by the circuit. Due to the fact that the optical output power of a diode laser is proportional to the injected current over the lasing threshold of the semiconductor at constant temperature [2], a powerful current source is demanded. Consequently, as system size is becoming smaller and smaller, less space for cooling is left. Less power can be dissipated and for higher output power the efficiency of the driver circuit must be increased. In brief, new circuit designs with higher efficiency for high output currents are required.

This thesis deals with investigations of applying switched power converters for that purpose. Especially the buck converter technology should be analyzed in detail and following research questions should be answered: How suitable is a conventional buck converter for driving high currents to a power laser diode and in which way can the converter topology be improved if appropriate? Typically, a buck converter is designed as a voltage source, so how well is the buck converter as a current source and what are the consequences? Moreover, what is the dynamic behaviour of the buck converter and how can the output current be controlled? All these questions will be discussed.
As a practical example, a high-power laser driver circuit should be designed for the tapered (TA) section of a high-brightness single-frequency distributed Bragg reflector (DBR) tapered diode laser [3] with an optical output power of $8W$ as shown in Fig. 1.1. For that purpose, the tapered section must be driven by a continuous-wave current up to $12.5A$. On the other hand, the circuit should also be designed to drive pulsed lasers in different applications. In total, the driver circuit should be capable to generate constant and pulsed laser currents up to $12.5A$ with a rise time of $10\mu s$.
The overall laser system is illustrated in Fig. 1.1, where the DBR tapered diode laser consists of a ridge waveguide (RW) section with DBR generating the laser beam and a tapered (TA) section amplifying it further. Both sections are driven separately, allowing beam quality and output power to be adjusted. Optionally, an

optical fiber may be connected to the high-power laser diode for some treatments. The investigations for this thesis were done in cooperation with Pantec Biosolutions AG, a leading company in the field of minimally invasive laser based medical engineering in Liechtenstein.

Low power lasers, as found in integrated optical communication and sensor systems [4, 5], are commonly driven by linear current regulators. In the middle power range, such as for driving the ridge waveguide (RW) section of the DBR tapered diode laser [3], more discrete linear regulators [6] are employed. Linear regulators have several advantages like high switching speed, small output current ripple, low component count and they can be integrated in CMOS technology in large quantities. Due to the fact that the excessive voltage is dissipated by a transistor to regulate the output current, the efficiency of the circuit is poor. Consequently, at high output currents large thermal power must be dissipated, which results in complex cooling systems, bigger size and finally in higher system costs.

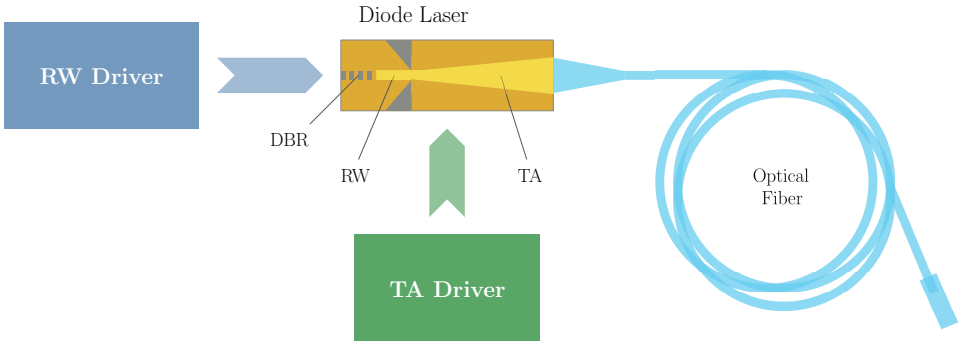

Figure 1.1.: Schematic illustration of the laser system

For driving high currents in power laser diodes, switched power converters are usually a better choice. Conventional buck converters are designed as voltage sources equipped with a buffer capacitor at the output. As a result, buck converter based laser drivers typically suffer from high output current ripple. In [7] an active ripple cancellation circuit was introduced to reduce the output ripple current to less than 1%. The ripple cancellation was designed as a linear regulator, which operates up to $2.5A$ at low losses. A buck converter with 3^{rd} order output filter for a laser current up to $50A$ was mentioned in [8]. The additional filter order reduces the ripple of the output current, but also causes an overshoot in the transient response. For high-power laser diodes, a multi-phase buck converter [9] can overcome the limiting factor of the heat produced in the output inductor. As the output current of the converter is distributed among the power stages, the size of the inductor in each power stage can be reduced. This results in higher power density and better efficiency. Moreover, the phase-shifted currents of each power stage are summed up, which increases the total switching frequency and lowers the magnitude of the current ripple. In pulsed laser systems, the switching frequency of a buck converter can be synchronized to

the repetition rate of the laser pulses [10]. The inductor current and accordingly the current ripple is synchronized to the laser pulses. Therefore, the pulse energy is kept constant, which is adequate in some applications. However, in continuous-wave and pulsed operation all these solutions are not optimal, thus further research should be done in this field.

An overview of the thesis is given in this section. In chapter 2, dynamic modeling of buck converters based on averaged state-space modeling is treated. Conventional buck converters in continuous- and discontinuous conduction mode are modeled first. For modeling the full dynamic behaviour of a current controlled buck converter, the load must be taken into account. By applying the two-port network theory, the control-to-output and line-to-output transfer functions of the current controlled buck converter are determined next. With these transfer functions, the dynamic behaviour for controller design and the filter characteristics for output current can be analyzed. It is shown that the output filter order of a conventional buck converter is reduced when the load becomes low-resistance, as it is the case for a high-power laser diode. Consequently, an additional inductor is added to the buck converter's output for improving the filter characteristics. The higher order buck converter is simply modeled by extending the conventional buck converter using the two-port network theory. Based on the modeling results, the higher order buck converter should be much better for filtering the laser current.
In order to compare the modeling results with measurements, a buck converter with 3^{rd} order output filter was implemented as described in chapter 3. The buck converter was designed with an integrated gallium nitride (GaN) half-bridge from EPC and an LCL low-pass output filter, operating at a switching frequency of $1MHz$. The control signals for the half-bridge are thereby generated by an FPGA. Additionally, an EMI filter was implemented to reduce electromagnetic interferences.
In chapter 4, the investigations of buck converters for driving high-power laser diodes are performed on an actual implementation of a $8W$ DBR tapered laser diode [3]. The dynamic modeling is verified first on a buck converter with a resistive load, as the high-power laser diode was modeled by a resistor at the operation point. Thereafter, buck converters driving the tapered section of a high-power DBR tapered laser diode and the impact of their non-linear load are analyzed. Measurements of the dynamic transient responses of the output currents 1^{st}, 2^{nd} and 3^{rd} order buck converters are therefore compared to the step responses of the modeled control-to-output transfer functions. It turned out that the inductance of the load's connecting wires is always present and should be considered. Accordingly, a conventional buck converter 2^{nd} order becomes practical a 3^{rd} order buck converter. Moreover, measurements of the output current ripple are performed and the filtering characteristics of the 1^{st}, 2^{nd} and 3^{rd} order output filters of buck converters are compared. As shown, a buck converter 3^{rd} order and accordingly a 2^{nd} order buck converter with wire inductance are significantly better for filtering the output current. Finally, the controller design complexity is contrasted with the output current filtering characteristics of the 1^{st}, 2^{nd} and 3^{rd} order buck converters for future implementations.

2. Dynamic Modeling

Modeling the dynamic behaviour of a switched power converter is essential for a detailed analysis [11]. In order to analyze and optimize the transient response of a power converter, the control-to-output transfer function must be determined. Based on that, the controller design is usually done. Moreover, analyzing the filtering characteristics of a converter can be performed on the line-to-output transfer function. Consequently, modeling the dynamic behaviour is indispensable for designing a power converter.
For modeling a buck converter, the basic operation principle must be understood. In the beginning, the basic operation of a buck converter will be discussed. Thereafter, the dynamic modeling of the buck converter in continuous- and discontinuous conduction mode will be done. To model the full dynamic behaviour of a buck converter, the load must be taken into account. The modeling of the current controlled buck converter with a laser diode as a load will be treated next. Out of the results obtained, the capacitor at the output of a conventional buck converter is not optimal for filtering the laser current. However, to overcome this drawback, the order of the output filter will be increased by an additional inductor. Finally, the corresponding higher order current controlled buck converter will be modeled and analyzed.

2.1. Basic Operation of a Buck Converter

In this section, the basic operation principle of a buck converter will be discussed. Therefore, steady-state condition is assumed, the dynamic modeling of the transients will be treated later. The content is based on [12] and more fundamentals are found in [11].

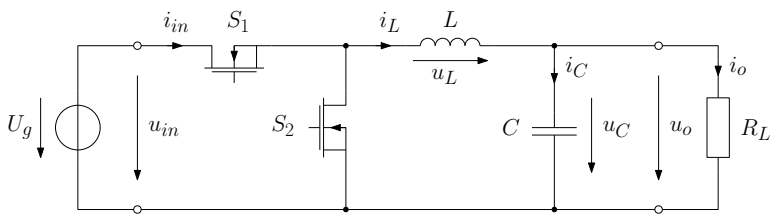

Figure 2.1.: Schematics of a buck converter

The basic circuit of a buck converter is shown in Fig. 2.1. The electrically controlled switches S_1 and S_2 are ideal and all component losses are neglected for simplification. A constant voltage source U_g provides the input voltage u_{in}, which is converted by the circuit to a lower output voltage u_o. Therefore, the output load is represented by a simple resistance R_L. Since the buck converter's function is to produce dc output, the output voltage consists of a desired dc and small ac portion. Due to the very small ac to dc proportion, typically smaller than 1%, the output ripple, which is produced by switching can be neglected for some calculations.

If we assume steady-state operation, the inductor current i_L and the capacitor voltage u_C are periodical over one switching cycle T_s. For ideal capacitors and inductors, the average inductor voltage $\langle u_L \rangle$ and average capacitor current $\langle i_C \rangle$ are zero over T_s.

$$\langle u_L \rangle = \frac{1}{T_s} \int_{t_0}^{T_s+t_0} u_L(t)\, dt = 0 \qquad (2.1) \qquad \langle i_C \rangle = \frac{1}{T_s} \int_{t_0}^{T_s+t_0} i_C(t)\, dt = 0 \qquad (2.2)$$

In Power Electronics, Eq. (2.1) and (2.2) are known as the principles of Inductor Volt-Second Balance and Capacitor Charge Balance [11]. It states that voltage time during charging equals voltage time during discharging in an inductor. For a capacitor, the total charge over one switching periode is zero. As a result, no energy is stored in an ideal inductor or capacitor over a switching cycle.
In **continuous conduction mode** (CCM), the switch S_1 is turned on and S_2 is turned off at the beginning of a switching cycle at time t_0. After some time t_{on}, smaller than T_s, the switch S_1 is turned off and S_2 is turned on again. Consequently, the circuit is running in two different operation modes, in Mode 1 for time t_{on} and in Mode 2 for time t_{off}. As a result, T_s can be described as a sum of t_{on} and t_{off}.

$$T_s = t_{on} + t_{off} \qquad (2.3)$$

Typically, the duty cycle D is used to describe t_{on} and t_{off} compared to T_s. The duty cycle is defined as the ratio of on-time to switching period in the range of $0 \leq D \leq 1$.

$$D = \frac{t_{on}}{T_s} \qquad (2.4)$$

Now, the on-time can be formulated as Eq. (2.5). Combining Eq. (2.3) and (2.4) leads to Eq. (2.6), which can be also formulated by the complement of the duty ratio D'.

$$t_{on} = DT_s \qquad (2.5)$$

$$t_{off} = (1 - D)T_s = D'T_s \qquad (2.6)$$

$$D' = 1 - D \qquad (2.7)$$

Next, we will analyze the two operation modes, Mode 1 and 2 more in detail. During t_{on} in Mode 1 switch S_1 is conducting and S_2 is blocked. Thus, the circuit in Fig. 2.1 can be simplified to Fig. 2.2.

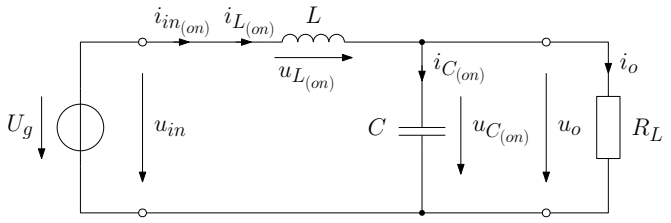

Figure 2.2.: Simplified schematics of a buck converter in Mode 1 for time t_{on}

$$u_{L_{(on)}} = u_{in} - u_o \quad (2.8) \qquad i_{C_{(on)}} = i_{L_{(on)}} - i_o \quad (2.9) \qquad i_{in_{(on)}} = i_{L_{(on)}} \quad (2.10)$$

Out of the simplified circuit for time t_{on}, we obtain Eq. (2.8), (2.9), (2.10) by using basic circuit theory. By applying the derivative form of the capacitor and inductor equation (2.11) and (2.12), we get Eq. (2.13) and (2.14).

$$u_L(t) = L\,\frac{di_L(t)}{dt} \quad (2.11) \qquad i_C(t) = C\,\frac{du_C(t)}{dt} \quad (2.12)$$

$$\frac{di_{L_{(on)}}}{dt} = \frac{u_{in} - u_o}{L} \quad (2.13) \qquad \frac{du_{C_{(on)}}}{dt} = \frac{i_{L_{(on)}} - i_o}{C} \quad (2.14)$$

Integrating Eq. (2.13) from $t = 0$ to t with the initial condition $i_L(0)$, we obtain $i_{L_{(on)}}$. That implies the inductor current rises linearly with a slope of $(u_{in} - u_o)/L$, where $i_L(0)$ is the initial value at $t = 0$.

$$i_{L_{(on)}}(t) = \int_0^t \frac{u_{in} - u_o}{L}\,dt = \frac{u_{in} - u_o}{L}\,t + i_L(0) \quad (2.15)$$

In Mode 2 for time t_{off}, when switch S_1 is off and S_2 is on, the circuit in Fig. 2.1 is simplified to Fig. 2.3. The voltage supply u_{in} is not connected at one side, so the circuit is not closed, and the voltage supply can be ignored for operation.

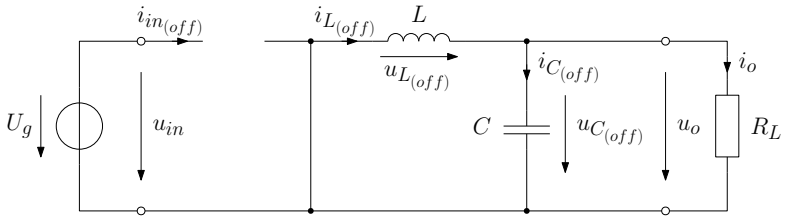

Figure 2.3.: Simplified schematics of a buck converter in Mode 2 for time t_{off}

$$u_{L_{(off)}} = -u_o \quad (2.16) \qquad i_{C_{(off)}} = i_{L_{(off)}} - i_o \quad (2.17) \qquad i_{in_{(off)}} = 0 \quad (2.18)$$

From the simplified circuit for time t_{off}, Eq. (2.16), (2.17) and (2.18) are found. By using Eq. (2.11) and (2.12), the following equations can be determined like before.

$$\frac{di_{L_{(off)}}}{dt} = \frac{-u_o}{L} \qquad (2.19) \qquad \frac{du_{C_{(off)}}}{dt} = \frac{i_{L_{(off)}} - i_o}{C} \qquad (2.20)$$

Integrating Eq. (2.19) from $t_{on} = DT_s$ to t with the starting condition $i_L(DT_s)$, we obtain $i_{L_{(off)}}$ which describes the descending curve of inductance current when the switches are changing from state 1 to 2.

$$i_{L_{(off)}}(t) = \int_{t_{on}}^{t} \frac{-u_o}{L}\, dt = \frac{-u_o}{L}\,(t - DT_s) + i_L(DT_s) \qquad (2.21)$$

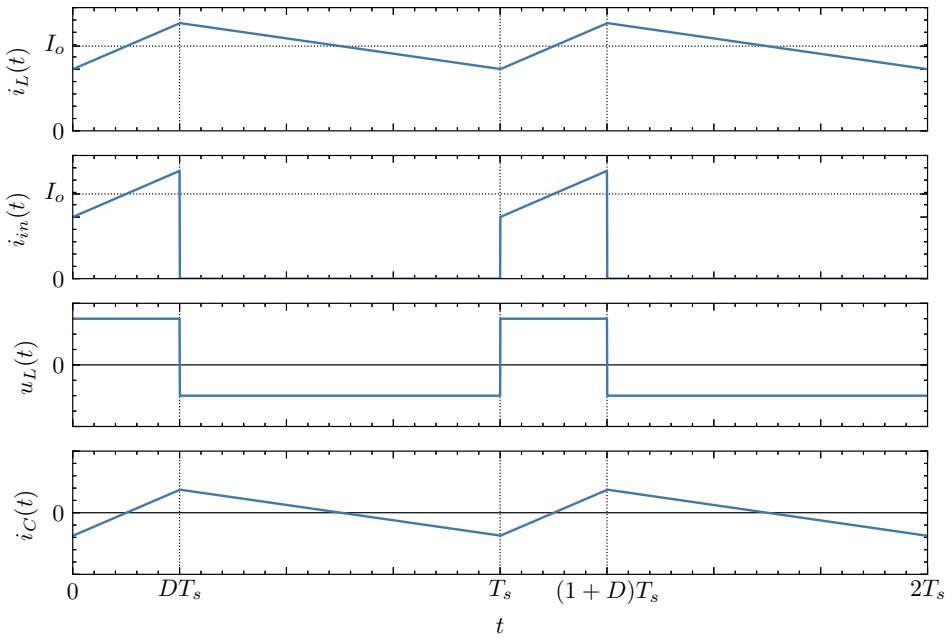

Figure 2.4.: Voltage and current waveforms of an ideal buck converter in continuous conduction mode

To determine the maximum inductance current $i_{L_{max}}$, time $t = DT_s$ is inserted in Eq. (2.15). The minimum inductance current $i_{L_{min}}$ is obtained by inserting $t = T_s$ in Eq. (2.21).

$$i_{L_{max}} = i_L(DT_s) = \frac{u_{in} - u_o}{L}\, DT_s + i_L(0) \qquad (2.22)$$

$$i_{L_{min}} = i_L(T_s) = \frac{-u_o}{L}\, D'T_s + i_L(DT_s) \qquad (2.23)$$

In steady-state operation, the inductor current after one periode T_s has to be the same. That relation is described in Eq. (2.24). Inserting Eq. (2.22) in (2.23) and applying Eq. (2.7) and (2.24) gives the output to input voltage ratio in Eq. (2.25).

$$i_L(0) = i_L(T_s) \qquad (2.24)$$

$$\frac{u_o}{u_{in}} = D \tag{2.25}$$

The output to input voltage ratio, also called voltage conversion ratio M in Eq. (2.25) is the fact why the circuit is known as the buck converter. The input voltage u_{in} is converted down to the output voltage u_o by the duty cycle value D.
To investigate the current conversion ratio we need to calculate the averaged input $\langle i_{in} \rangle$ and output $\langle i_o \rangle$ currents first. That is done by integrating both currents over one switching period and dividing them by T_s. The averaging of i_{in} was determined by integrating Eq. (2.10) and (2.18) over t_{on} and t_{off}, sum them up and divide the result by T_s. For $\langle i_o \rangle$ the output current i_o is needed, by applying the capacitor charge balance in Eq. (2.2) the averaged output current has to be the same as the averaged inductance current. Now, the averaging can be done like before. By inserting Eq. (2.22) and (2.23), the result can be simplified to Eq. (2.26) and (2.27). Note that the averaging can be determined too by calculating the area under the waveforms in Fig. 2.4.

$$\langle i_{in} \rangle = \frac{1}{T_s} \int_0^{T_s} i_{in}(t)\, dt = \frac{D}{2} \left(i_{L_{max}} + i_{L_{min}} \right) \tag{2.26}$$

$$\langle i_o \rangle = \frac{1}{T_s} \int_0^{T_s} i_o(t)\, dt = \frac{1}{2} \left(i_{L_{max}} + i_{L_{min}} \right) \tag{2.27}$$

In steady-state operation, $\langle i_{in} \rangle$ and $\langle i_o \rangle$ are constant over time and can be described as I_{in} and I_o. Therefore, the current conversion ratio is determined out of Eq. (2.26) and (2.27) and simplified to Eq. (2.28). Combining the voltage and current conversion ratio leads to Eq. (2.29).

$$\frac{I_o}{I_{in}} = \frac{1}{D} \tag{2.28}$$

$$M = \frac{U_o}{U_{in}} = \frac{I_{in}}{I_o} = D \tag{2.29}$$

Eq. (2.29) means that the input voltage of a buck converter is converted down to the output voltage by the duty cycle D. At the same time, the output current is converted up by D. As a result, the input and output power of an ideal buck converter are the same, and the circuit is operating like an ideal transformer.

The voltage and current waveforms of an ideal buck converter in continuous conduction mode are shown in Fig. 2.4. The inductor current was drawn out from Eq. (2.15) and (2.21). Since the switch S_1 is just on at t_{on}, the circuit consumes current during that time. Consequently, the input current is zero during t_{off}. Out of Eq. (2.8) and (2.16) the inductor voltage was determined. Finally, the capacitor current is the inductance current subtracted by the output current as defined in Eq.(2.9) and (2.17).

In continuous conduction mode (CCM), the inductor current is always larger than zero in steady-state operation. If the inductance of the inductor L becomes smaller and smaller, the inductor current decreases and reaches zero during a switching

period T_s. Now, the buck converter is operating in discontinuous conduction (DCM) mode. The boundary between these two modes of operation occurs when the inductor current goes to zero at T_s. To determine the inductor value at this point, we insert Eq. (2.27) to (2.23), applying $I_o = \frac{U_o}{R_L}$ and setting the result to zero. That leads to the following critical inductor value L_{crit}.

$$L_{crit} = \frac{D'T_s}{2} R_L \tag{2.30}$$

As a result, the operation mode of an ideal buck converter depends on the inductor value L, the load resistance R_L, the duty cycle D and the switching frequency $T_s = \frac{1}{f_s}$, and must be evaluated separately for each application. On the other hand, the operation mode can be selected by the inductor value L.

In **discontinuous conduction mode** (DCM), the properties of a buck converter change significantly. In this section, the buck converter will be considered more closely in that operation mode. Typically, in DCM the switch S_2 is replaced by a diode D in reverse direction as shown in Fig. 2.5.

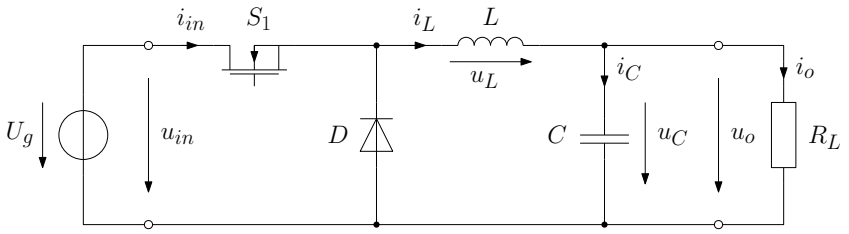

Figure 2.5.: Typical schematics of a buck converter in discontinuous conduction mode

In DCM, there exists one more mode of operation compared to the CCM discussed earlier. If the inductor current i_L goes to zero, the diode D is blocking and the current stays zero until the end of the switching cycle. The additional Mode 3 occurs when i_L is zero. In Fig. 2.6 the simplified circuit in Mode 3 is shown.

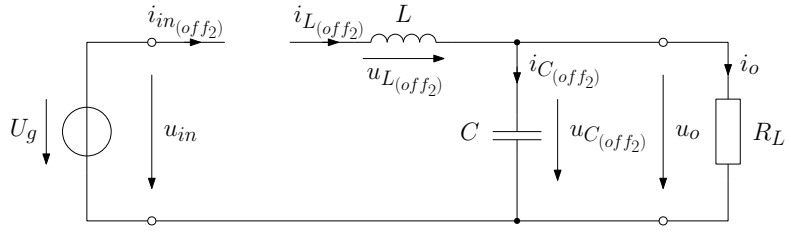

Figure 2.6.: Simplified schematics of a buck converter in Mode 3 for $i_L = 0$

$$u_{L_{(off_2)}} = 0 \qquad (2.31) \qquad i_{C_{(off_2)}} = -i_o \qquad (2.32) \qquad i_{in_{(off_2)}} = 0 \qquad (2.33)$$

Combining all three modes of operation, we can draw the voltage and current waveforms of an ideal buck converter in discontinuous conduction mode in Fig. 2.7. Note that the inductance current goes to zero during a switching period and starts at zero each time.

Now, the voltage and current conversion ratios will be determined in the discontinuous conduction mode. By inserting $t = DT_s$ in Eq. (2.15) and $t = D_1T_s$ in Eq. (2.21) we obtain the new $I_{L_{max}}$ and $I_{L_{min}}$ values. Due to the operation mode $i_L(0)$ and $I_{L_{min}}$ are zero. By applying Eq. (2.34) to (2.35), we get the voltage conversion ratio in Eq. (2.36).

$$i_{L_{max}} = i_L(DT_s) = \frac{u_{in} - u_o}{L} DT_s \tag{2.34}$$

$$i_{L_{min}} = i_L(D_1T_s) = \frac{-u_o}{L}(D_1 - D)T_s + i_L(DT_s) = 0 \tag{2.35}$$

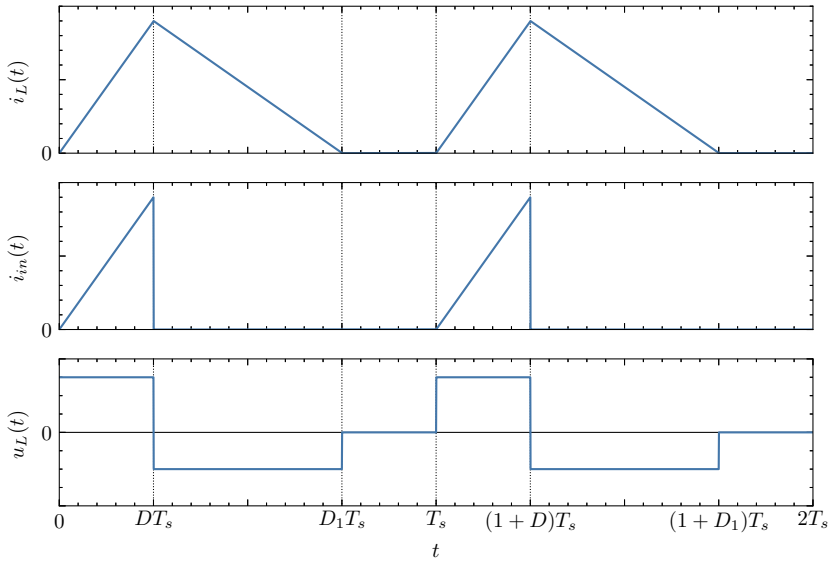

Figure 2.7.: Voltage and current waveforms of a buck converter in discontinuous conduction mode

$$M = \frac{U_o}{U_{in}} = \frac{D}{D_1} \tag{2.36}$$

The voltage conversion ratio is given by the known duty cycle D and the unknown value of D_1, so D_1 has to be defined first. In an ideal buck converter, the input power P_{in} and the output power P_{out} must be the same. By applying $P = UI$ to Eq. (2.37), $I_o = \frac{U_o}{R_L}$ and Eq. (2.26) with $i_{L_{min}} = 0$, a new relation for $i_{L_{max}}$ is found. Substituting this equation into Eq. (2.35) results in Eq. (2.38).

$$P_{in} = P_{out} \tag{2.37}$$

$$D_1 = \frac{2LU_o}{DT_sR_LU_{in}} + D \tag{2.38}$$

Inserting Eq. (2.38) into the voltage conversion ratio in Eq. (2.36) gives a quadratic equation, which can be converted to Eq. (2.39). By using the normalized time constant $\tau_n = \frac{\tau}{T}$ with $\tau = \frac{L}{R}$ the voltage conversion ratio is simplified further. Out of Eq. (2.37) the current conversion ratio in Eq. (2.40) can be found.

$$M = \frac{D^2 T_s R_L}{4L}\left(\sqrt{1+\frac{8L}{D^2 T_s R_L}}-1\right) = \frac{D^2}{4\tau_n}\left(\sqrt{1+\frac{8\tau_n}{D^2}}-1\right) \tag{2.39}$$

$$M = \frac{U_o}{U_{in}} = \frac{I_{in}}{I_o} \tag{2.40}$$

As a result, the voltage conversion ratio in DCM becomes nonlinear and depends not only on D, but also on the component values L, R_L and the switching period T_s. Therefore, it is obvious that the dynamics of an ideal buck converter in DCM changes significantly compared to CCM.

2.2. Dynamic Modeling of a Buck Converter

Modeling the dynamic behaviour of a buck converter in continuous- and discontinuous conduction mode will be discussed now. In continuous conduction mode, dynamic modeling dates back to the 1970s, whereby the transient behaviour was fully described [13]. More than 20 years later, the buck convert in discontinuous conduction mode was modeled completely for the first time [14].
Two main types of models exist for modeling the dynamics of a power converter. The models are given either in analytical form or as equivalent circuits [13, 14]. In analytical form, the model is based on the state-space averaging approach, where the state-space representation of all operation modes are averaged over one switching cycle. On the other hand, in the equivalent circuit canonical model the averaged properties of a power converter are represented in a single linear circuit. In this thesis the focus is laid on the averaged state-space modeling.

2.2.1. Overview of the Modeling Approach

In this section, a short overview of the general modeling approach of the averaged state-space model is given. Note, that this approach is valid generally in continuous- and discontinuous conduction mode [13, 14].

In the first step, the state-space equations of the simplified circuits in each switching mode are determined separately. In each state, all equations of the Kirchhoff's voltage

and current laws are derived out of the simplified circuit. By applying the derivative form of the capacitor and inductor equation, the derived equations can be transformed into the state-space representation [15]. The state-space model is typically described in matrix form as shown in Eq. (2.41) and (2.42).

$$\frac{d\mathbf{x}(t)}{dt} = \mathbf{A}\mathbf{x}(t) + \mathbf{B}\mathbf{u}(t) \tag{2.41}$$

$$\mathbf{y}(t) = \mathbf{C}\mathbf{x}(t) + \mathbf{D}\mathbf{u}(t) \tag{2.42}$$

In the state-space representation, the state vector $\mathbf{x}(t)$ contains all state variables of a system. The state variables are often given by the storage elements, which are in the case of electrical circuits the capacitor voltages and the inductor currents. Moreover, the total number of the storage elements defines the order of the system. The input signals are given by the input vector $\mathbf{u}(t)$. All elements in the matrices **A**,**B**,**C** and **D** are time independent and constant values. Finally, the output signals are described by the vector $\mathbf{y}(t)$.

Next, the state-space models of all switching states must be averaged and combined. Time-averaging is commonly done over all n switching states in a switching periode T_S as mentioned first in [16]. Therefore, the state-space equations of each switching mode are multiplied by their duration time t_n and then they are summed up. Subsequently, the result is divided by the total switching periode $T_S = t_1 + \cdots + t_n$. In compact form that can be expressed by the following equations.

$$\frac{d\langle\mathbf{x}\rangle}{dt} = \frac{1}{T_s}\left(t_1 \cdot \frac{d\mathbf{x}_1}{dt} + \cdots + t_n \cdot \frac{d\mathbf{x}_n}{dt}\right) \tag{2.43}$$

$$\langle\mathbf{y}\rangle = \frac{1}{T_s}\left(t_1 \cdot \mathbf{y}_1 + \cdots + t_n \cdot \mathbf{y}_n\right) \tag{2.44}$$

The averaged state-space models of power converters are frequently nonlinear [13, 14]. For further analysis, the state-space equations must be linearized. In control engineering, linearization is usually achieved by a linear approximation in a specific operation point, where the higher-order terms of the Taylor series expansion are neglected [15]. If we consider the state-space equations as nonlinear functions $\frac{d\mathbf{x}}{dt} = \mathbf{f}(\mathbf{x},\mathbf{u})$ and $\mathbf{y} = \mathbf{g}(\mathbf{x},\mathbf{u})$, the system can be linearized in the operation point **X** and **U** by following equations.

$$\frac{d\hat{\mathbf{x}}}{dt} = \left.\frac{\partial\mathbf{f}}{\partial\mathbf{x}}\right|_{\substack{\mathbf{x}=\mathbf{X}\\\mathbf{u}=\mathbf{U}}} \hat{\mathbf{x}} + \left.\frac{\partial\mathbf{f}}{\partial\mathbf{u}}\right|_{\substack{\mathbf{x}=\mathbf{X}\\\mathbf{u}=\mathbf{U}}} \hat{\mathbf{u}} \tag{2.45}$$

$$\hat{\mathbf{y}} = \left.\frac{\partial \mathbf{g}}{\partial \mathbf{x}}\right|_{\substack{\mathbf{x}=\mathbf{X}\\ \mathbf{u}=\mathbf{U}}} \hat{\mathbf{x}} + \left.\frac{\partial \mathbf{g}}{\partial \mathbf{u}}\right|_{\substack{\mathbf{x}=\mathbf{X}\\ \mathbf{u}=\mathbf{U}}} \hat{\mathbf{u}} \tag{2.46}$$

Finally, the transfer functions are derived from the linearized state-space representation. By applying the Laplace transformation, Eq. (2.41) and (2.42) are transformed from linear differentials to algebraic equations. Now, the equations can be combined and rearranged to the transfer functions $\mathbf{G}(s)$, which are obtained by dividing the output signals $\mathbf{Y}(s)$ by the input signals $\mathbf{U}(s)$. In brief, the transfer functions can be determined from the state-space model as follows.

$$\mathbf{G}(s) = \frac{\mathbf{Y}(s)}{\mathbf{U}(s)} = \mathbf{C}\left(s\mathbf{I} - \mathbf{A}\right)^{-1}\mathbf{B} + \mathbf{D} \tag{2.47}$$

2.2.2. Buck Converter in Continuous Conduction Mode

The modeling of the dynamic behaviour of a buck converter in continuous conduction mode is treated now. For accurate modeling of the dynamics, the component losses must be taken into account. In Fig. 2.8 additional resistors are added to the ideal buck converter of Fig. 2.1 to represent the losses in a more practical way. This section is based on [13, 17, 18].

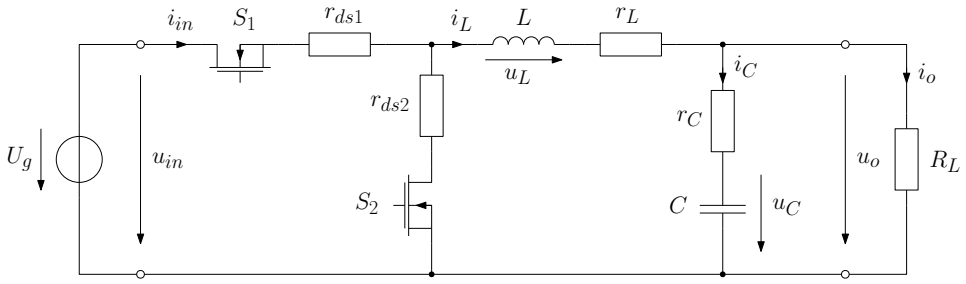

Figure 2.8.: Schematics of a buck converter in CCM with component losses

To analyze the buck converter in more detail, the circuit is divided into the different modes of operation. First Mode 1 for time t_{on} will be examined. The simplified circuit for this mode is shown in Fig. 2.9.

By determining the Kirchhoff's voltage and current laws of Fig. 2.9 (as found in Appendix A.1) and applying the derivative form of the capacitor voltage and the inductor current of Eq. (2.11) and (2.12), the state-space equations (2.48) to (2.51) are derived.

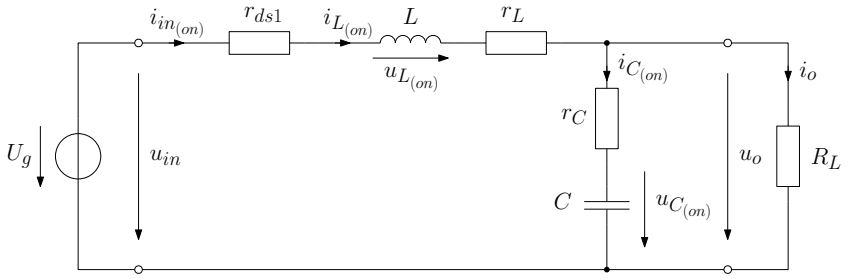

Figure 2.9.: Simplified schematics of a buck converter with component losses in Mode 1 for time t_{on}

$$\frac{di_{L_{(on)}}}{dt} = -\frac{r_{ds1} + r_L + r_C}{L} i_{L_{(on)}} - \frac{1}{L} u_{C_{(on)}} + \frac{1}{L} u_{in_{(on)}} + \frac{r_C}{L} i_o \tag{2.48}$$

$$\frac{du_{C_{(on)}}}{dt} = \frac{1}{C} i_{L_{(on)}} - \frac{1}{C} i_o \tag{2.49}$$

$$i_{in_{(on)}} = i_{L_{(on)}} \tag{2.50}$$

$$u_{o_{(on)}} = u_{C_{(on)}} + r_C C \frac{du_{C_{(on)}}}{dt} \tag{2.51}$$

As next step, the same calculations are done for time t_{off} in Mode 2. Therefore, the simplified circuit is shown in Fig. 2.10 and the derived state-space equations are described in Eq. (2.52) to (2.55). The Kirchhoff's voltage and current laws of Fig. 2.10 can be found in the Appendix A.1 like before.

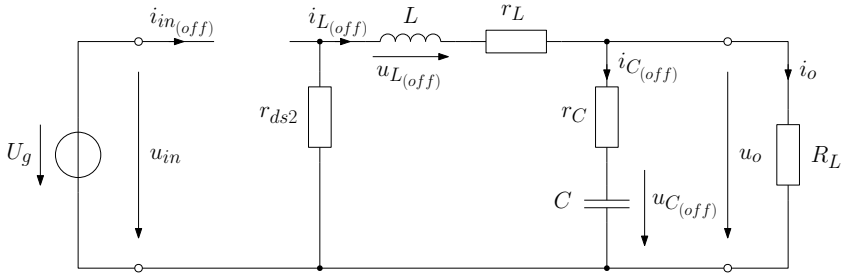

Figure 2.10.: Simplified schematics of a buck converter with component losses in Mode 2 for time t_{off}

$$\frac{di_{L_{(off)}}}{dt} = -\frac{r_{ds2} + r_L + r_C}{L} i_{L_{(off)}} - \frac{1}{L} u_{C_{(off)}} + \frac{r_C}{L} i_o \tag{2.52}$$

$$\frac{du_{C_{(off)}}}{dt} = \frac{1}{C} i_{L_{(off)}} - \frac{1}{C} i_o \tag{2.53}$$

$$i_{in_{(off)}} = 0 \tag{2.54}$$

$$u_{o_{(off)}} = u_{C_{(off)}} + r_C\, C\, \frac{du_{C_{(off)}}}{dt} \tag{2.55}$$

Next, the two switching modes must be averaged over one switching period T_s. The averaging is done by multiplying the on-time equations (2.48) to (2.51) by t_{on} and Eq. (2.52) to (2.55) by t_{off}, summing up the results and dividing by T_s. By applying Eq. (2.5) to (2.7), the averaged equations can be described in terms of the duty cycle d as follows. Note, that d is lower case to indicate that the variable is time varying.

$$\frac{d\langle i_L\rangle}{dt} = -\frac{r_L + r_C + d\, r_{ds1} + d' r_{ds2}}{L}\langle i_L\rangle - \frac{1}{L}\langle u_C\rangle + \frac{d}{L}\langle u_{in}\rangle + \frac{r_C}{L}\langle i_o\rangle \tag{2.56}$$

$$\frac{d\langle u_C\rangle}{dt} = \frac{1}{C}\langle i_L\rangle - \frac{1}{C}\langle i_o\rangle \tag{2.57}$$

$$\langle i_{in}\rangle = d\langle i_L\rangle \tag{2.58}$$

$$\langle u_o\rangle = \langle u_C\rangle + r_C\, C\, \frac{d\langle u_C\rangle}{dt} \tag{2.59}$$

Due to the product of two time varying variables, such as $d\langle i_L\rangle$ and $d\langle u_{in}\rangle$, Eq. (2.56) to (2.59) are nonlinear and must be linearized. By forming the partial derivatives to all time varying input and state variables in the operation point and summing them up as stated in Eq. (2.45) and (2.46), results in the linearized equations (2.60) to (2.63). The upper case letters indicate the operation point, where the linearization is performed. By setting the derivatives of the averaged state variables in (2.56) and (2.57) to zero, the operation points in Eq. (2.64) to (2.67) are derived.

$$\begin{aligned}\frac{d\hat{i}_L}{dt} = &-\frac{r_L + r_C + D r_{ds1} + D' r_{ds2}}{L}\,\hat{i}_L - \frac{1}{L}\,\hat{u}_C + \frac{D}{L}\,\hat{u}_{in} + \frac{r_C}{L}\,\hat{i}_o \\ &+ \frac{U_{in} + (r_{ds1} - r_{ds2}) I_o}{L}\,\hat{d}\end{aligned} \tag{2.60}$$

$$\frac{d\hat{u}_C}{dt} = \frac{1}{C}\,\hat{i}_L - \frac{1}{C}\,\hat{i}_o \tag{2.61}$$

$$\hat{i}_{in} = D\,\hat{i}_L + I_L\,\hat{d} \tag{2.62}$$

$$\hat{u}_o = \hat{u}_C + r_C\, C\, \frac{d\hat{u}_C}{dt} \tag{2.63}$$

$$I_L = I_o \qquad (2.64) \qquad U_C = U_o \qquad (2.65) \qquad I_{in} = DI_L \qquad (2.66)$$

$$D = \frac{U_o + I_o(r_L + r_{ds2})}{U_{in} + I_o(r_{ds2} - r_{ds1})} \qquad (2.67)$$

Now, Eq. (2.60) to (2.63) are represented in the state-space matrix form in Eq. (2.70) and (2.71). By using the Laplace transformation, the transfer function $\mathbf{G}(s)$ is determined out of the state-space representation by Eq. (2.47). That results in Eq. (2.72), where $\Delta(s)$ is the characteristic polynomial of the matrix $\mathbf{A}$.

$$r_1 = r_L + r_C + Dr_{ds1} + D'r_{ds2} \qquad (2.68) \qquad U_1 = U_{in} + (r_{ds1} - r_{ds2})I_o \qquad (2.69)$$

$$\frac{d}{dt}\underbrace{\begin{bmatrix}\hat{i}_L\\ \hat{u}_C\end{bmatrix}}_{\mathbf{x}} = \underbrace{\begin{bmatrix}-\frac{r_1}{L} & -\frac{1}{L}\\ \frac{1}{C} & 0\end{bmatrix}}_{\mathbf{A}}\underbrace{\begin{bmatrix}\hat{i}_L\\ \hat{u}_C\end{bmatrix}}_{\mathbf{x}} + \underbrace{\begin{bmatrix}\frac{D}{L} & \frac{r_C}{L} & \frac{U_1}{L}\\ 0 & -\frac{1}{C} & 0\end{bmatrix}}_{\mathbf{B}}\underbrace{\begin{bmatrix}\hat{u}_{in}\\ \hat{i}_o\\ \hat{d}\end{bmatrix}}_{\mathbf{u}} \qquad (2.70)$$

$$\underbrace{\begin{bmatrix}\hat{i}_{in}\\ \hat{u}_o\end{bmatrix}}_{\mathbf{y}} = \underbrace{\begin{bmatrix}D & 0\\ 0 & 1 + r_C C\frac{d}{dt}\end{bmatrix}}_{\mathbf{C}}\underbrace{\begin{bmatrix}\hat{i}_L\\ \hat{u}_C\end{bmatrix}}_{\mathbf{x}} + \underbrace{\begin{bmatrix}0 & 0 & I_o\\ 0 & 0 & 0\end{bmatrix}}_{\mathbf{D}}\underbrace{\begin{bmatrix}\hat{u}_{in}\\ \hat{i}_o\\ \hat{d}\end{bmatrix}}_{\mathbf{u}} \qquad (2.71)$$

$$\begin{bmatrix}\hat{i}_{in}\\ \hat{u}_o\end{bmatrix} = \frac{1}{\Delta(s)}\begin{bmatrix}\frac{D^2}{L}s & \frac{D}{LC}(1 + sr_C C) & \frac{DU_1}{L}s + I_o\Delta(s)\\ \frac{D}{LC}(1 + sr_C C) & \frac{1}{LC}(1 + sr_C C)(r_C - r_1 - sL) & \frac{U_1}{LC}(1 + sr_C C)\end{bmatrix}\begin{bmatrix}\hat{u}_{in}\\ \hat{i}_o\\ \hat{d}\end{bmatrix} \qquad (2.72)$$

$$\Delta(s) = det\,(s\mathbf{I} - \mathbf{A}) = s^2 + \frac{r_1}{L}s + \frac{1}{LC} \qquad (2.73)$$

The matrix in Eq. (2.72) describes the averaged dynamic behaviour of a buck converter in continuous conduction mode. From the two-port network theory [19] it is clear that the result can be represented by g-parameters. This leads to the more general form in Eq. (2.74). The two-port network representation is convenient for further analysis.

$$\begin{bmatrix}\hat{i}_{in}\\ \hat{u}_o\end{bmatrix} = \begin{bmatrix}g_{11} & g_{12} & g_{13}\\ g_{21} & g_{22} & g_{23}\end{bmatrix}\begin{bmatrix}\hat{u}_{in}\\ \hat{i}_o\\ \hat{d}\end{bmatrix} \qquad (2.74)$$

$$g_{11} = \left.\frac{\hat{i}_{in}}{\hat{u}_{in}}\right|_{\hat{i}_o=\hat{d}=0} \quad (2.75) \qquad g_{12} = \left.\frac{\hat{i}_{in}}{\hat{i}_o}\right|_{\hat{u}_{in}=\hat{d}=0} \quad (2.76) \qquad g_{13} = \left.\frac{\hat{i}_{in}}{\hat{d}}\right|_{\hat{u}_{in}=\hat{i}_o=0} \quad (2.77)$$

$$g_{21} = \left.\frac{\hat{u}_o}{\hat{u}_{in}}\right|_{\hat{i}_o=\hat{d}=0} \quad (2.78) \qquad g_{22} = \left.\frac{\hat{u}_o}{\hat{i}_o}\right|_{\hat{u}_{in}=\hat{d}=0} \quad (2.79) \qquad g_{23} = \left.\frac{\hat{u}_o}{\hat{d}}\right|_{\hat{u}_{in}=\hat{i}_o=0} \quad (2.80)$$

2.2.3. Buck Converter in Discontinuous Conduction Mode

For modeling the dynamics of a buck converter in discontinuous conduction mode, the circuit in Fig. 2.11 is used. Resistors are added to the ideal buck converter in Fig. 2.5 to represent the component losses. This chapter is based on [14, 17, 18].

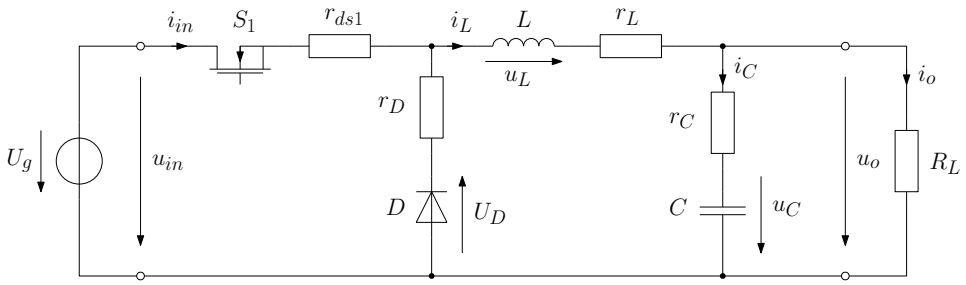

Figure 2.11.: Schematics of a buck converter in DCM with component losses

Now, the buck converter is divided into the different operation modes for a detailed analyze. First Mode 1 for time t_{on} will be examined, which is identical to CCM. The simplified circuit for Mode 1 can be found in Fig. 2.9 and the following equations were derived. Note, m_1 is defined as the slope of i_L for time t_{on}.

$$\frac{di_{L_{(on)}}}{dt} = -\frac{r_{ds1} + r_L + r_C}{L}\, i_{L_{(on)}} - \frac{1}{L}\, u_{C_{(on)}} + \frac{1}{L}\, u_{in_{(on)}} + \frac{r_C}{L}\, i_o = m_1 \quad (2.81)$$

$$\frac{du_{C_{(on)}}}{dt} = \frac{1}{C}\, i_{L_{(on)}} - \frac{1}{C}\, i_o \quad (2.82)$$

$$i_{in_{(on)}} = i_{L_{(on)}} \quad (2.83)$$

$$u_{o_{(on)}} = u_{C_{(on)}} + r_C\, C\, \frac{du_{C_{(on)}}}{dt} \quad (2.84)$$

Next, the analysis is done for Mode 2, the first part t_{off1} of the off-time. That leads to the simplified circuit in Fig. 2.12 and the corresponding equations. The Kirchhoff's voltage and current laws are given in the Appendix A.1.

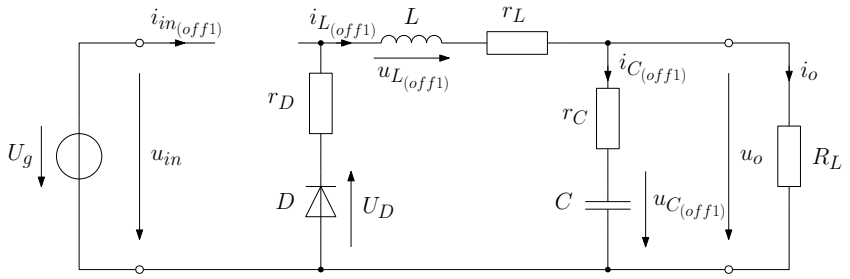

Figure 2.12.: Simplified schematics of a buck converter in DCM with component losses in Mode 2

$$\frac{di_{L_{(off1)}}}{dt} = -\frac{r_D + r_L + r_C}{L}\, i_{L_{(off1)}} - \frac{1}{L}\, u_{C_{(off1)}} + \frac{r_C}{L}\, i_o - \frac{U_D}{L} = m_2 \tag{2.85}$$

$$\frac{du_{C_{(off1)}}}{dt} = \frac{1}{C}\, i_{L_{(off1)}} - \frac{1}{C}\, i_o \tag{2.86}$$

$$i_{in_{(off1)}} = 0 \tag{2.87}$$

$$u_{o_{(off1)}} = u_{C_{(off1)}} + r_C\, C\, \frac{du_{C_{(off1)}}}{dt} \tag{2.88}$$

The second part t_{off2} of the off-time, Mode 3, will be analyzed now. No current i_L is flowing in this mode and the circuit can be simplified to Fig. 2.13.

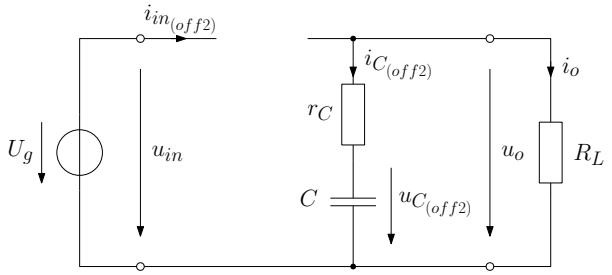

Figure 2.13.: Simplified schematics of a buck converter in DCM with component losses in Mode 3

$$\frac{di_{L_{(off2)}}}{dt} = 0 \tag{2.89}$$

$$\frac{du_{C_{(off2)}}}{dt} = -\frac{1}{C}\, i_o \tag{2.90}$$

$$i_{in_{(off2)}} = 0 \tag{2.91}$$

$$u_{o_{(off2)}} = u_{C_{(off2)}} + r_C\, C\, \frac{du_{C_{(off2)}}}{dt} \tag{2.92}$$

Now, the averaging over one switching period must be adapted to the inductor current in DCM. Therefore, the inductor current i_L is shown in Fig. 2.14. During t_{on} and t_{off1} the inductor current is flowing, but during t_{off2} it is zero. As a result, one more equation is required to define t_{off1} or t_{off2}. Based on the waveform in Fig. 2.14, the maximum inductor current in Eq. (2.93) can be determined by the current slope m_1 and the on-time t_{on}. The area under the current curve i_L divided by T_s gives the averaged inductor current in Eq. (2.94). Combining these two equations and using $t_{on} = dT_s$ and $t_{off1} = d_1 T_s$ leads to the duty cycle d_1 for time t_{off1} in Eq. (2.95). This result is helpful to substitute the unknown duty cycle d_1 in further calculations [14].

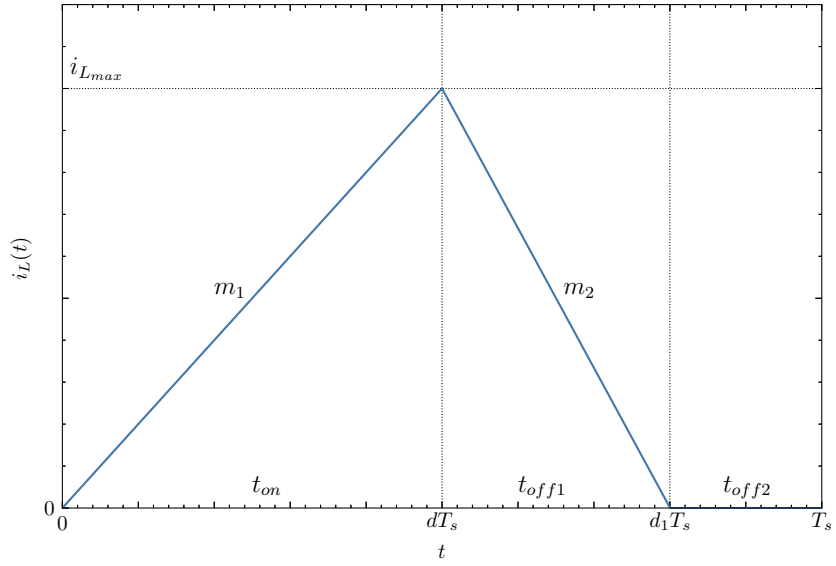

Figure 2.14.: Inductor current waveform in DCM

$$i_{L_{max}} = m_1\, t_{on} \tag{2.93}$$

$$\langle i_L \rangle = \frac{1}{T_s} \int_0^{T_s} i_L(t)\, dt = \frac{i_{L_{max}}}{2T_s} \left(t_{on} + t_{off1} \right) \tag{2.94}$$

$$d_1 = \frac{2\langle i_L \rangle}{m_1 d T_s} - d \tag{2.95}$$

The averaging is performed by multiplying the slopes of the different modes of operation by their on- and off-times, summing them up and dividing the result by the switching cycle. In terms of the duty cycle, the averaged equations can be formulated as follows. By inserting Eq. (2.95) and applying the slopes m_1 of Eq. (2.81) and m_2 of Eq. (2.85), the Eq. (2.100) to (2.103) are determined.

$$\frac{d\langle i_L\rangle}{dt} = m_1 d + m_2 d_1 \tag{2.96}$$

$$\frac{d\langle u_C\rangle}{dt} = \frac{1}{C}\langle i_L\rangle - \frac{1}{C}\langle i_o\rangle \tag{2.97}$$

$$\langle i_{in}\rangle = \frac{d}{d+d_1}\langle i_L\rangle \tag{2.98}$$

$$\langle u_o\rangle = \langle u_C\rangle + r_C\, C\, \frac{d\langle u_C\rangle}{dt} \tag{2.99}$$

$$\begin{aligned}\frac{d\langle i_L\rangle}{dt} = {} & \frac{d(r_D - r_{ds1})}{L}\langle i_L\rangle + \frac{d}{L}\langle u_{in}\rangle + \frac{dU_D}{L} \\ & + \frac{2\langle i_L\rangle}{dT_s}\,\frac{(r_L + r_C + r_D)\langle i_L\rangle + \langle u_C\rangle + U_D - r_C\langle i_o\rangle}{(r_L + r_C + r_{ds1})\langle i_L\rangle + \langle u_C\rangle - \langle u_{in}\rangle - r_C\langle i_o\rangle}\end{aligned} \tag{2.100}$$

$$\frac{d\langle u_C\rangle}{dt} = \frac{1}{C}\langle i_L\rangle - \frac{1}{C}\langle i_o\rangle \tag{2.101}$$

$$\langle i_{in}\rangle = -\frac{d^2 T_s}{2L}\Big((r_L + r_C + r_{ds1})\langle i_L\rangle + \langle u_C\rangle - \langle u_{in}\rangle - r_C\langle i_o\rangle\Big) \tag{2.102}$$

$$\langle u_o\rangle = \langle u_C\rangle + r_C\, C\, \frac{d\langle u_C\rangle}{dt} \tag{2.103}$$

Next, Eq. (2.100) to (2.103) are linearized in the steady-state operation point. The operation point there can be specified by setting the derivatives of Eq. (2.100) and (2.101) to zero, which yields to the following equations.

$$I_L = I_o \tag{2.104}$$

$$U_C = U_o \tag{2.105}$$

$$I_{in} = I_o\,\frac{U_1}{U_2} \tag{2.106}$$

$$D = \sqrt{\frac{2L}{T_s}\,\frac{I_{in}}{-U_3}} \tag{2.107}$$

$$U_1 = (r_L + r_D)I_o + U_o + U_D \quad (2.108) \qquad U_2 = (r_D - r_{ds1})I_o + U_{in} + U_D \quad (2.109)$$

$$U_3 = (r_L + r_{ds1})I_o + U_o - U_{in} \quad (2.110) \qquad r_1 = r_L + r_C + r_{ds1} \quad (2.111)$$

The linearization of Eq. (2.100) to (2.103) are performed in the same manner as in the continuous conduction mode. That results in large equations, which can be represented in the state-space matrix in Eq. (2.112) and (2.113) in compact form.

$$\underbrace{\frac{d}{dt}\begin{bmatrix}\hat{i}_L \\ \hat{u}_C\end{bmatrix}}_{\mathbf{x}} = \underbrace{\begin{bmatrix}a_{11} & a_{12} \\ a_{21} & a_{22}\end{bmatrix}}_{\mathbf{A}}\underbrace{\begin{bmatrix}\hat{i}_L \\ \hat{u}_C\end{bmatrix}}_{\mathbf{x}} + \underbrace{\begin{bmatrix}b_{11} & b_{12} & b_{13} \\ b_{21} & b_{22} & b_{23}\end{bmatrix}}_{\mathbf{B}}\underbrace{\begin{bmatrix}\hat{u}_{in} \\ \hat{i}_o \\ \hat{d}\end{bmatrix}}_{\mathbf{u}} \quad (2.112)$$

$$\underbrace{\begin{bmatrix}\hat{i}_{in} \\ \hat{u}_o\end{bmatrix}}_{\mathbf{y}} = \underbrace{\begin{bmatrix}c_{11} & c_{12} \\ c_{21} & c_{22}\end{bmatrix}}_{\mathbf{C}}\underbrace{\begin{bmatrix}\hat{i}_L \\ \hat{u}_C\end{bmatrix}}_{\mathbf{x}} + \underbrace{\begin{bmatrix}d_{11} & d_{12} & d_{13} \\ d_{21} & d_{22} & d_{23}\end{bmatrix}}_{\mathbf{D}}\underbrace{\begin{bmatrix}\hat{u}_{in} \\ \hat{i}_o \\ \hat{d}\end{bmatrix}}_{\mathbf{u}} \quad (2.113)$$

$$a_{11} = \frac{D}{L}(r_D - r_{ds1}) + \frac{2}{DT_s}\left(\frac{(r_L + r_C + r_D)I_o\Big((r_1 - 2r_C)I_o + 2(U_o - U_{in})\Big)}{U_3^2} + \frac{(U_o - U_{in} - r_C I_o)(U_o + U_D - r_C I_o)}{U_3^2}\right)$$

$$a_{12} = -\frac{2I_o}{DT_s}\frac{U_2}{U_3^2} \qquad a_{21} = \frac{1}{C} \qquad a_{22} = b_{21} = b_{23} = 0$$

$$b_{11} = \frac{D}{L} + \frac{2I_o}{DT_s}\frac{U_1}{U_3^2} \qquad b_{12} = \frac{2I_o}{DT_s}\frac{U_2}{U_3^2}r_C \qquad b_{13} = \frac{U_2}{L} - \frac{2I_o}{D^2T_s}\frac{U_1}{U_3}$$

$$b_{22} = -\frac{1}{C} \qquad c_{11} = -\frac{D^2T_s}{2L}r_1 \qquad c_{12} = -\frac{D^2T_s}{2L}$$

$$c_{21} = 0 \qquad c_{22} = 1 + r_C C\frac{d}{dt} \qquad d_{11} = \frac{D^2T_s}{2L}$$

$$d_{12} = \frac{D^2T_s}{2L}r_C \qquad d_{13} = -\frac{DT_s}{L}U_3 \qquad d_{21} = d_{22} = d_{23} = 0$$

By using Eq. (2.47) and the Laplace transformation, the transfer function $\mathbf{G}(s)$ is determined out of the state-space matrix form. This leads to the same g-parameter representation as in Eq. (2.74) and describes the dynamic behaviour of the buck converter in discontinuous conduction mode. Note that solving the transfer functions in analytical form is not practical as it results in huge equations. In some special cases it can be simplified further or computed numerically.

2.3. Modeling of a Current Controlled Buck Converter

For modeling the full dynamic behaviour of a buck converter the load must be taken into account. Depending on the nature of the load, a current is flowing at a certain output voltage of a buck converter. The modeling of the buck converter with a diode load and how the output current is determined will be discussed here. Moreover, for the controller design of a current controlled buck converter the control-to-output transfer function, more precisely the output current to duty cycle transfer function of the circuit is needed. On the other hand, analyzing the filtering characteristics of a buck converter can be performed in detail on the line-to-output transfer function. The modeling of a current controlled buck converter and the derivation of the corresponding transfer functions based on the two-port network theory [19] are discussed now.

High-power laser diodes behave electrically similar to semiconductor power diodes [3]. In the operation point a power laser diode can be modeled by a resistor r_D, which is obtained by the voltage to current ratio in Eq. (2.114) out of the static characteristic diode curve. The electrical model of the diode can be represented in a-parameter matrix form in Eq. (2.115) as shown in Fig. 2.15. For determination Eq. (2.116) to (2.118) are applied. Note that the size of the matrix is 3×3, which is handy for the matrix multiplication in the next steps.

$$r_D = \left.\frac{U_D}{I_D}\right|_Q \tag{2.114}$$

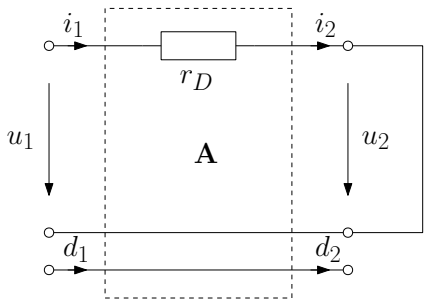

$$\begin{bmatrix} u_1 \\ i_1 \\ d_1 \end{bmatrix} = \begin{bmatrix} 1 & r_D & 0 \\ 0 & 1 & 0 \\ 0 & 0 & 1 \end{bmatrix} \begin{bmatrix} u_2 \\ i_2 \\ d_2 \end{bmatrix} \tag{2.115}$$

Figure 2.15.: Matrix representation of the diode

$$u_1 = u_2 + r_D i_2 \qquad (2.116) \qquad i_1 = i_2 \qquad (2.117) \qquad d_1 = d_2 \qquad (2.118)$$

As the resistance of a power laser diode is typically low-ohmic at the operation point [3], the buck converter is operating in CCM. Thus, the modeling is based on the buck converter in CCM. The dynamic behaviour of a buck converter in CCM is defined by the g-parameter matrix in Eq. (2.72). To combine the matrices of the buck converter and the diode load, the g-parameter matrix in Eq. (2.72) is transformed to the a-parameter form by following equation.

$$\begin{bmatrix} \hat{u}_{in} \\ \\ \hat{i}_{in} \end{bmatrix} = \frac{1}{g_{21}} \begin{bmatrix} 1 & -g_{22} & -g_{23} \\ \\ g_{11} & g_{12}g_{21} - g_{11}g_{22} & g_{13}g_{21} - g_{11}g_{23} \end{bmatrix} \begin{bmatrix} \hat{u}_o \\ \hat{i}_o \\ \hat{d} \end{bmatrix} \qquad (2.119)$$

Now, the a-parameter matrix of the buck converter and the matrix of the diode load can be combined by a matrix multiplication [19]. That results in a new a-parameter matrix of size 2×3. To determine the output current to duty cycle transfer function the y-parameter matrix is of assistance [20]. Therefore, the combined matrix is converted by Eq. (2.120) to the y-parameter matrix in Eq. (2.121).

$$\begin{bmatrix} \hat{i}_{in} \\ \\ \hat{i}_o \end{bmatrix} = \frac{1}{a_{12}} \begin{bmatrix} a_{22} & a_{12}a_{21} - a_{11}a_{22} & a_{12}a_{23} - a_{13}a_{22} \\ \\ 1 & -a_{11} & -a_{13} \end{bmatrix} \begin{bmatrix} \hat{u}_{in} \\ \hat{u}_o \\ \hat{d} \end{bmatrix} \qquad (2.120)$$

$$\begin{bmatrix} \hat{i}_{in} \\ \\ \hat{i}_o \end{bmatrix} = \begin{bmatrix} y_{11} & y_{12} & y_{13} \\ \\ y_{21} & y_{22} & y_{23} \end{bmatrix} \begin{bmatrix} \hat{u}_{in} \\ \hat{u}_o \\ \hat{d} \end{bmatrix} \qquad (2.121)$$

$$y_{11} = \left.\frac{\hat{i}_{in}}{\hat{u}_{in}}\right|_{\hat{u}_o=\hat{d}=0} \qquad (2.122) \qquad y_{12} = \left.\frac{\hat{i}_{in}}{\hat{u}_o}\right|_{\hat{u}_{in}=\hat{d}=0} \qquad (2.123) \qquad y_{13} = \left.\frac{\hat{i}_{in}}{\hat{d}}\right|_{\hat{u}_{in}=\hat{u}_o=0} \qquad (2.124)$$

$$y_{21} = \left.\frac{\hat{i}_o}{\hat{u}_{in}}\right|_{\hat{u}_o=\hat{d}=0} \qquad (2.125) \qquad y_{22} = \left.\frac{\hat{i}_o}{\hat{u}_o}\right|_{\hat{u}_{in}=\hat{d}=0} \qquad (2.126) \qquad y_{23} = \left.\frac{\hat{i}_o}{\hat{d}}\right|_{\hat{u}_{in}=\hat{u}_o=0} \qquad (2.127)$$

Consequently, the matrix element y_{23} in Eq. (2.127) represents exactly the desired transfer function. The output current to duty cycle transfer function $P(s)$ in Eq. (2.128) of the current controlled buck converter was determined analytically by the computer algebra system Maxima, an open source descendant of Macsyma [21], in that way.

$$P(s) = \frac{i_o}{d} = \frac{U_1 \left(1 + r_c C\, s\right)}{\left(r_C + r_D\right) LC\, s^2 + \left(L + \left(\left(r_C + r_D\right) r_1 - r_C^2\right) C\right) s + r_1 + r_D - r_C} \qquad (2.128)$$

If we assume that the drain to source resistance of both switches S_1 and S_2 of the buck converter are the same, Eq. (2.128) can be simplified further. That results in Eq. (2.129), which is interestingly independent of the operation point of the buck converter.

$$P(s) = \frac{U_{in}\,(1 + r_c C\,s)}{(r_C + r_D)\,LC\,s^2 + \left(L + \left((r_C + r_D)\,(r_L + r_C + r_{ds}) - r_C^2\right) C\right) s + r_L + r_{ds} + r_D} \tag{2.129}$$

For a detailed analysis, it is more handy to represent the transfer function in the general form in Eq. (2.130). The transfer function $P(s)$ consists of a first order high-pass filter polynomial in the numerator, a second order low-pass filter polynomial in the denominator and the gain A. The second order low-pass is defined by the cutoff frequency ω_1 and the damping ratio d. The first order high-pass filter is fully described by the cutoff frequency ω_2.

$$P(s) = A_1 \frac{1 + \frac{s}{\omega_2}}{s^2 + 2d\omega_1 s + \omega_1^2} \tag{2.130}$$

$$A_1 = \frac{U_{in}}{r_C + r_D}\frac{1}{LC} \qquad \omega_1 = \sqrt{\frac{1}{LC}\frac{r_L + r_{ds} + r_D}{r_C + r_D}} \qquad \omega_2 = \frac{1}{r_C C}$$

$$d = \frac{1}{2\omega_1}\left(\frac{r_L + r_C + r_{ds}}{L} - \frac{r_C^2}{L(r_C + r_D)} + \frac{1}{C(r_C + r_D)}\right)$$

To find the filtering characteristics of a buck converter, the same y-parameter matrix representation can be used. The matrix element y_{21} in Eq. (2.125) gives the output current to input voltage transfer function $G(s)$. Modeling the dynamic behaviour of the buck converter, the switching characteristics was lost by averaging the signals over a switching cycle. On the other hand the switching characteristics of S_1 and S_2 can be considered as a square wave input voltage with duty cycle d. Accordingly, the output current to input voltage transfer function in Eq (2.131) describes the filtering characteristics of a buck converter. From a comparison of Eq. (2.131) and (2.128), it is clear that the frequency behaviour of $G(s)$ and $P(s)$ are the same. As a result the output current to input voltage transfer function can be represented in a much simpler form in Eq. (2.132).

$$G(s) = \frac{i_o}{u_{in}} = \frac{D\,(1 + r_c C\,s)}{(r_C + r_D)\,LC\,s^2 + \left(L + \left((r_C + r_D)\,r_1 - r_C^2\right) C\right) s + r_1 + r_D - r_C} \tag{2.131}$$

$$G(s) = A_2 \frac{1 + \frac{s}{\omega_2}}{s^2 + 2d\omega_1 s + \omega_1^2} \tag{2.132} \qquad A_2 = \frac{D}{(r_C + r_D)LC}$$

For driving high-power laser diodes, the transient behaviour of a buck converter should be sufficiently fast to reach a new operation point, but at the same time the output ripple current in steady-state should be as small as possible. This means theoretically, that frequencies lower than the selected cutoff frequency ω_c should be generated by the buck converter, but frequencies higher than ω_c should be blocked completely. In practice the cutoff frequency ω_c must be selected as low as possible and the order of the buck converter defines the attenuation of the harmonics. Furthermore, the switching frequency f_s should be as fast as practicable for low output ripple. Related to the transfer function $G(s)$, this implies that the cutoff frequency ω_1 of the low-pass filter is selected according to the application and the frequency ω_2 of the high-pass filter must be as high as possible. Therefore, the resistance r_C of the output capacitor must be small. As the resistance of a power laser diode becomes lower and lower, the term of the squared Laplace variable s^2 in the denominator of Eq. (2.129) decreases until it vanishes completely. As a result, for high laser currents, the resistance r_C becomes very low-ohmic and the transfer functions $P(s)$ and $G(s)$ are simplified further to Eq. (2.133) and (2.134).

$$P(s) = \frac{A_3}{1 + \frac{s}{\omega_3}} \qquad (2.133) \qquad\qquad G(s) = \frac{A_4}{1 + \frac{s}{\omega_3}} \qquad (2.134)$$

$$A_3 = \frac{U_{in}}{r_L + r_{ds} + r_D} \qquad\qquad A_4 = \frac{D}{r_L + r_{ds} + r_D}$$

$$\omega_3 = \frac{r_L + r_{ds} + r_D}{L}$$

Summarized, when the load impedance of a current controlled buck converter becomes low-resistance, the order of the output filter is effectively reduced from second to first order. This implies that the capacitor on the output of a buck converter has little impact on the filtering characteristics of higher output currents. As a result, the output current ripple becomes triangle-shaped and usually fairly large. Consequently, for driving power laser diodes, the current controlled buck converter is not optimal and further improvements should be done.

2.4. Modeling of a Higher Order Current Controlled Buck Converter

To improve the filtering of the output current, the filter order of a buck converter can be increased. As mentioned before, the output capacitor has little effect on the filtering characteristics of a current controlled buck converter. Typically, a capacitor is applied for buffering voltages, but an inductor could be more effective for smoothing the output current. Hence an additional inductor is added to the output of the buck converter, resulting in a higher order output filter.
For modeling the dynamics of a higher order current controlled buck converter the matrix representation of the additional inductor must be found. In Fig. 2.16 the electrical model of the inductor is shown. Out of Fig. 2.16, Eq. (2.136) to (2.138) are derived, which can be represented in a-parameter matrix form in Eq. (2.135).

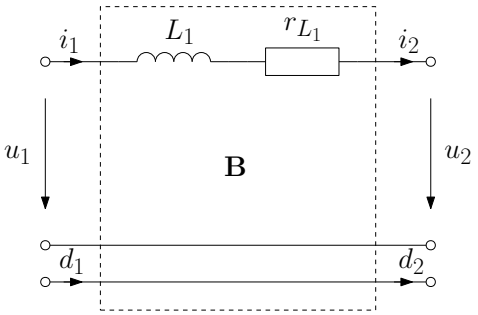

$$\begin{bmatrix} u_1 \\ i_1 \\ d_1 \end{bmatrix} = \begin{bmatrix} 1 & r_{L_1} + sL_1 & 0 \\ 0 & 1 & 0 \\ 0 & 0 & 1 \end{bmatrix} \begin{bmatrix} u_2 \\ i_2 \\ d_2 \end{bmatrix} \tag{2.135}$$

Figure 2.16.: Matrix representation of the inductor

$$u_1 = u_2 + (r_{L_1} + sL_1)\, i_2 \tag{2.136}$$

$$i_1 = i_2 \tag{2.137}$$

$$d_1 = d_2 \tag{2.138}$$

The dynamic modeling of the extended buck converter is done in a similar way as before. First, the a-parameter matrices of the buck converter **C** in CCM, the additional inductor **B** and the laser diode load **A** are combined by matrix multiplications as described in Eq. (2.139). The result **D** is converted by Eq. (2.120) to the y-parameter representation. The transfer functions $P(s)$ and $G(s)$ are determined by the matrix elements y_{23} and y_{21}. This yields to Eq. (2.140) and (2.143), which are closely resembling. Consequently, just one more matrix multiplication is required for modeling the higher order converter.

$$\mathbf{D} = \mathbf{C} \cdot \mathbf{B} \cdot \mathbf{A} \tag{2.139}$$

$$P(s) = \frac{i_o}{d} = \frac{U_1\,(1 + r_c C\, s)}{\begin{aligned} &LL_1C\, s^3 + \left(\left(r_{L_1} + r_C + r_D\right) L + r_1 L_1\right) C\, s^2 + \left(L + L_1\right. \\ &\left. + \left(\left(r_{L_1} + r_C + r_D\right) r_1 - r_C^2\right) C\right) s + r_{L_1} + r_1 + r_D - r_C \end{aligned}} \tag{2.140}$$

$$P(s) = \frac{U_{in}\,(1 + r_c C\,s)}{\begin{array}{l} L L_1 C\,s^3 + \left(\left(r_{L_1} + r_C + r_D\right) L + \left(r_L + r_C + r_{ds}\right) L_1\right) C\,s^2 + \big(L + L_1 \\ \quad + \left(\left(r_{L_1} + r_C + r_D\right)\left(r_L + r_C + r_{ds}\right) - r_C^2\right) C\big)\,s + r_L + r_{L_1} + r_{ds} + r_D \end{array}} \tag{2.141}$$

With the assumption of equal drain to source resistance of switch S_1 and S_2, the transfer function $P(s)$ is simplified further to Eq. (2.141). For simplicity, the ratio k is applied to describe L_1 in terms of L. Thus, the transfer function can be written in the general form in Eq. (2.142). As a result, the numerator of $P(s)$ is a polynomial of a high-pass first order and the denominator a low-pass polynomial of third order, so the order of the low-pass filter of the extended buck converter has increased by one.

$$P(s) = A_1\,\frac{1 + \frac{s}{\omega_2}}{s^3 + a\,s^2 + b\,s + \omega_1^3} \tag{2.142}$$

$$k = \frac{L_1}{L} \qquad A_1 = \frac{U_{in}}{kL^2C} \qquad \omega_1 = \sqrt[3]{\frac{1}{kL^2C}\Big(r_L + r_{L_1} + r_{ds} + r_D\Big)} \qquad \omega_2 = \frac{1}{r_C C}$$

$$a = \frac{1}{L}\Big(r_L + r_C + r_{ds} + \frac{1}{k}\big(r_{L_1} + r_C + r_D\big)\Big)$$

$$b = \frac{1}{kL^2}\left(\left(r_L + r_C + r_{ds}\right)\left(r_{L_1} + r_C + r_D\right) - r_C^2\right) + \frac{1}{LC}\left(1 + \frac{1}{k}\right)$$

$$G(s) = \frac{i_o}{u_{in}} = \frac{D\,(1 + r_c C\,s)}{\begin{array}{l} L L_1 C\,s^3 + \left(\left(r_{L_1} + r_C + r_D\right) L + r_1 L_1\right) C\,s^2 + \big(L + L_1 \\ \quad + \left(\left(r_{L_1} + r_C + r_D\right) r_1 - r_C^2\right) C\big)\,s + r_{L_1} + r_1 + r_D - r_C \end{array}} \tag{2.143}$$

$$G(s) = A_2\,\frac{1 + \frac{s}{\omega_2}}{s^3 + a\,s^2 + b\,s + \omega_1^3} \tag{2.144} \qquad A_2 = \frac{D}{kL^2C}$$

Finally, the filtering characteristics of the higher order current controlled buck converter is analyzed. The output current to input voltage transfer function in Eq. (2.143) is described in the general form in Eq. (2.144). It can easily be recognized, that the order of the low-pass filter in the denominator has increased by one compared to the conventional current controlled buck converter. Moreover, the third-order term in Eq. (2.143) does not disappear if the load impedance becomes low-resistance. Consequently, for driving power laser diodes the output filter of the higher order current controlled buck converter should be much better for filtering the laser current.

3. Circuit Design

A buck converter with 3^{rd} order output filter was implemented to compare the modeling results with actual measurements. The buck converter was designed with an integrated GaN half-bridge [22] from EPC and an LCL low-pass output filter, operating at a switching frequency of $1MHz$. The control signals for the half-bridge are thereby generated by an FPGA. Additionally, an EMI filter was designed to reduce the electromagnetic interferences caused by switching the input current from the buck converter. The implementation of all these subsystems is covered in this chapter.

In the picture of Fig. 3.1, the implemented buck converter with PCB dimensions of $7.5cm \times 6cm$ is shown. The circuit is powered by a voltage of $12V$ at the connector on left and the tapered section of the DBR tapered laser diode [3] is connected to the screw terminals on right hand side. Finally, an FPGA evaluation board is connected to the box header on top side.

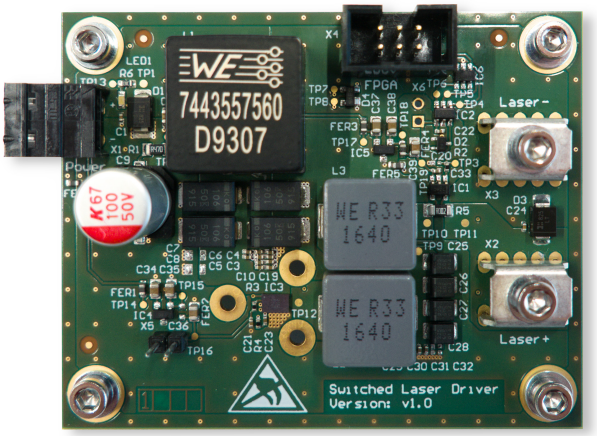

Figure 3.1.: Picture of the implemented buck converter

3.1. System Overview

First, an overview of the operation principle of the overall system is given. Thereafter, the functioning and design of the subsystems are discussed in detail. In Fig. 3.2 an overview of the system is shown.

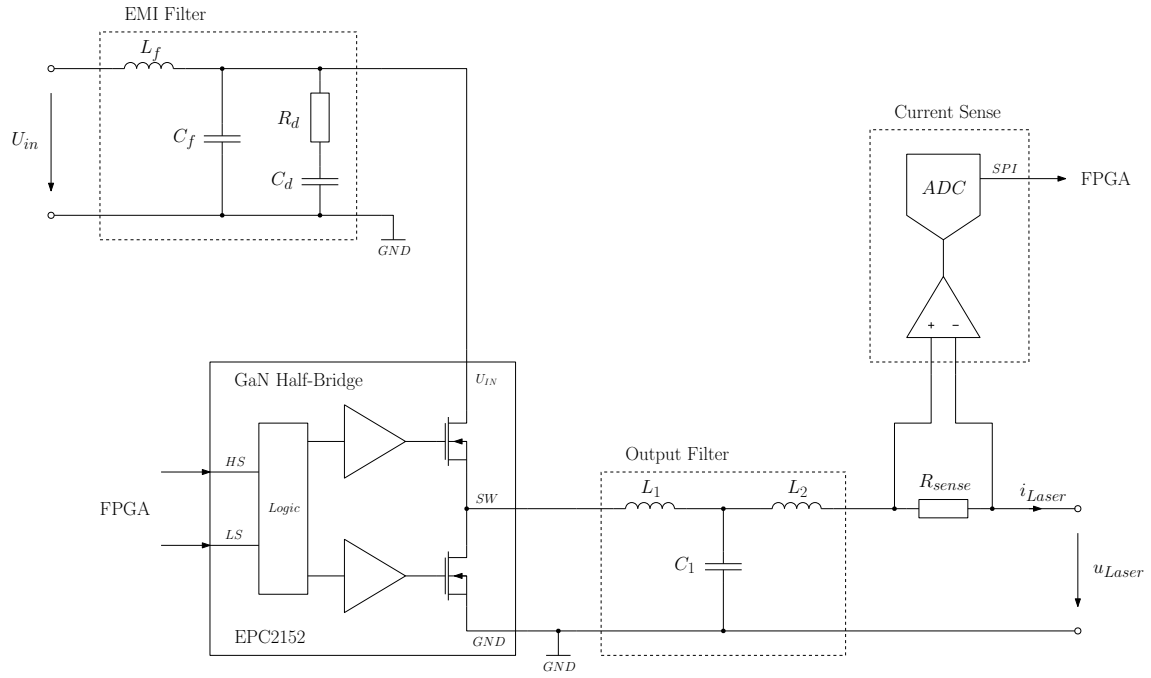

Figure 3.2.: System overview of the implemented buck converter

The buck converter 3^{rd} order mainly consists of the *EPC*2152 [22], a GaN half-bridge with integrated gate driver from EPC and an LCL low-pass output filter. For controlling the high- and low-side FETs of the half-bridge with requisite dead times, the signals are generated with an Intel Cyclone 10*LP* FPGA on an additional evaluation board. The GaN half-bridge is powered with an input voltage of $12V$, which is filtered by an EMI filter. Electromagnetic interferences are especially caused by the fast switching input current of a buck converter. To prevent them from spreading, they are filtered by the EMI filter as close as practicable to the GaN half-bridge. For a subsequent controller design, a sense resistor with amplifier and ADC is provided to measure the current flowing through the laser diode. The sampled current values are transmitted then via SPI protocol to the FPGA. Since the controller design is beyond the scope of this thesis, the functionality of the current measurement circuit is not discussed in more detail.

3.2. Buck Converter Design

Several steps are required to practically design a buck converter. Initially, the maximum values of the components must be estimated. Thereafter, the components can be selected for the half-bridge and the output filter. The buck converter is assembled and put into operation afterwards. The major steps are now treated more precisely.

3.2.1. Determination of the Maximum Values

Determining the maximum values in the circuit is essential for designing a solid buck converter. The maximum voltage and current values should never exceed the rated component values in long-term operation. Moreover, the thermal losses in the components must remain under their thermal limits, otherwise they will be destroyed. Hence, the maximum values of a conventional buck converter are determined now.

To estimate the maximum values, it is adequate to consider the ideal buck converter. Therefore, the component values are determined from the two operation modes in Fig. 2.2 and 2.3 of the ideal buck converter in Fig. 2.1. Therefrom, the following maximum voltage and current values can be found, whereby the inductor ripple current amplitude ΔI_L is applied for simplicity.

$$U_{S_{1(max)}} = U_{S_{2(max)}} = U_{in_{(max)}} \tag{3.1}$$

$$I_{S_{1(max)}} = I_{S_{2(max)}} = I_{L_{(max)}} \tag{3.2}$$

$$U_{C_{(max)}} = U_{o_{(max)}} \tag{3.3}$$

$$I_{C_{(max)}} = 2\,\Delta I_{L_{(max)}} \tag{3.4}$$

The peak-to-peak ripple current amplitude ΔI_{Lpp} is determined from Eq. (2.22) by setting $i_L(0)$ to zero. Consequently, the inductor ripple current amplitude ΔI_L is half of the peak-to-peak value. Moreover, the maximum inductor current $I_{L_{(max)}}$ can be defined as following.

$$\Delta I_{L_{pp}} = \frac{U_{in} - U_o}{L}\, DT_s \tag{3.5}$$

$$\Delta I_L = \frac{\Delta I_{L_{pp}}}{2} \tag{3.6}$$

$$I_{L_{(max)}} = I_{o_{(max)}} + \Delta I_{L_{(max)}} \tag{3.7}$$

In order to determine the thermal losses in the components, the root mean square values of the currents are convenient. Therefore, the root mean square values are calculated now for the current waveforms in Fig. 2.4. As shown, the inductor current ripple is triangular shaped. Correspondingly, the root mean square value is deter-

mined by $\frac{1}{\sqrt{3}}$ of the ripple current amplitude. The root mean square inductor current is thus given by Eq. 3.9.

$$\Delta I_{L_{RMS}} = \frac{\Delta I_L}{\sqrt{3}} \tag{3.8}$$

$$I_{L_{RMS}} = I_o + \frac{\Delta I_L}{\sqrt{3}} \tag{3.9}$$

The root mean square value of the input current is determined by integrating the squared inductor current in Eq. 2.15 over $t_{on} = DT_s$, averaging the result over T_s and taking the square root. By applying Eq. (2.22), (2.23), $I_{L_{max}} = I_o + \Delta I_L$ and $I_{L_{min}} = I_o - \Delta I_L$ the equation is simplified further. Moreover, $I_{in_{RMS}}$ is equal to $I_{S_{1RMS}}$. Finally, the root mean square current $I_{S_{2RMS}}$ can be determined by Eq. 3.11.

$$I_{in_{RMS}} = \sqrt{\frac{1}{T_s}\int_0^{t_{on}} i^2_{L_{(on)}}(t)\,dt} = \sqrt{D\left(I_o^2 + \frac{1}{3}\Delta I_L^2\right)} \tag{3.10}$$

$$I_{S_{2RMS}} = I_{L_{RMS}} - I_{S_{1RMS}} = \sqrt{D'\left(I_o^2 + \frac{1}{3}\Delta I_L^2\right)} \tag{3.11}$$

Now that the maximum values and the root mean square currents have been determined, the components for the buck converter circuit can be selected.

3.2.2. GaN Half-Bridge Design

The arrangement of the switches in a buck converter, with high- and low-side FETs is often named half-bridge. Correspondingly, a simple and cost-effective solution was sought to implement a half-bridge. The decision was made for the *EPC*2152 [22], a gallium nitride (GaN) half-bridge from EPC. The properties of this integrated power stage are now described in more detail.

The *EPC*2152 is a GaN FET half-bridge power stage with included gate driver, bootstrap charging, level shifting and input logic circuits integrated within a monolithic chip. The functional block diagram of the *EPC*2152 is shown in Fig. 3.4. All these essential functions of a power stage are integrated in a single chip with dimensions of $3.9mm \times 2.6mm$, which is shown in Fig. 3.3. Accordingly, only a few extra components are needed.

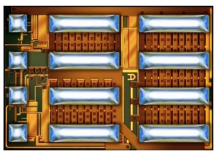

Figure 3.3.: Picture of the monolithic chip [23, Fig. 1.28]

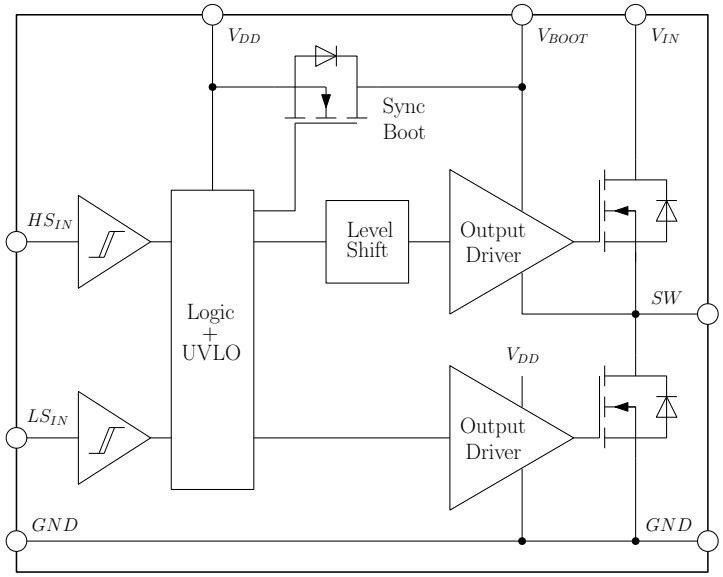

Figure 3.4.: Functional block diagram of the *EPC*2152 power stage [22]

The *EPC*2152 can deliver output currents of at least 12.5A continuously with an additional heat sink and can be powered with input voltages up to 60V. The *EPC*2152 operates up to a PWM switching frequency of 3MHz with switching times of 1ns under full load. Furthermore, the input logic interface of the *EPC*2152 can be connected directly to a digital controller. However, all these features are well suited for our application.

Nevertheless, the question remains why gallium nitride is used in this chip? Gallium nitride has some great electrical material properties compared to silicon. The bandgap energie of GaN is about 3 times higher than silicon. This results in lower leakage currents and higher operation temperatures in the power transistors. Moreover, the critical electric field is directly affected by the strength of the chemical bonds between the atoms in the lattice. The stronger bonds lead to a 10 times higher critical electrical field and therefore a breakdown by the avalanche effect occurs later at higher voltages. By the higher critical electrical field, the material thickness can be reduced by a factor of 10 for the same breakdown voltage. The distance between drain and source is reduced as well, resulting in a lower on-resistance. Consequently, GaN transistors have higher breakdown voltage, smaller on-resistance and are significantly smaller in size. Due to the smaller size, the parasitic capacitances in the FET are reduced, resulting in lower switching losses. Correspondingly, the switching frequency can be increased. Due to the fact that GaN FETs are typically grown on silicon substrate, various types of transistors can be combined on a wafer. As a result, CMOS logic, analog circuits and power FETs can be integrated in a single chip. In a power stage, such as the *EPC*2152, the integration of GaN FETs with gate drivers minimises common source inductance and gate drive loop inductance. Consequently, the switching frequency and the efficiency of the power stage are improved significantly. [23]

3.2.3. Output Filter Design

The filtering characteristics of a buck converter 3^{rd} order is described by the line-to-output transfer function in Eq. (2.144). For driving a high-power laser diode, the transient behaviour of a buck converter should be sufficiently fast for reaching a new operation point, but simultaneously the output current ripple should be as small as possible in steady-state. Accordingly, the output filter cut-off frequency ω_c must be selected as low as practicable and the filter order defines the attenuation of the switched PWM signal. Therefore, it would be practical if the cut-off frequency of the output filter could be specified. Based on the last term of the denominator in Eq. (2.144), the filter capacitor can be determined for a given cut-off frequency ω_c.

$$C = \frac{1}{\omega_c^3 k L^2}\Big(r_L + r_{L_1} + r_{ds} + r_D\Big) \tag{3.12}$$

A cut-off frequency f_c of $60kHz$ was selected for the output filter of the implemented buck converter, several times lower than the switching frequency of $1MHz$. Like this, the output filter is fast enough to achieve a requested rise time of $10\mu s$.

When selecting the capacitor, the nominal voltage and rated ripple current must be known. The maximum voltage on the capacitor can be determined by Eq. (3.3), whereby the additional voltage ripple should be considered. In any case, the nominal voltage should be selected higher than the maximum voltage with an extra safety margin. The ripple current in the capacitor is determined with Eq. (3.8). If the rated ripple current of a single capacitor is not large enough, multiple capacitors can be connected in parallel. Moreover, different types of capacitors may be combined to widen the frequency range for filtering.

The inductors of the output filter must also be selected appropriately. The saturation current must be higher than the maximum inductor current calculated by Eq. (3.7). Furthermore, the thermal heating of the inductors should not exceed a critical level. With Eq. (3.9) the current responsible for the heating is determined. Accordingly, a compatible inductor can be selected for this purpose.

3.3. EMI Filter Design

The input current of a buck converter is flowing into the circuit during time t_{on} and is zero during time t_{off} as shown in Fig. 2.4. Correspondingly, extremely short current rise times occur, which are equivalent to the switching times of the FETs. Electromagnetic interferences are caused by these current slopes. To prevent them

from spreading, the input current should be smoothed by an EMI filter as close as practicable to the power transistors.

An EMI filter is typically realized with an LC low-pass filter. The inductor thereby limits the current slope at the input and the capacitor provides the high current pulses for switching. In order to avoid the buck converter becoming unstable by the EMI filter, the LC low-pass filter must be damped around the cut-off frequency [11, 24].

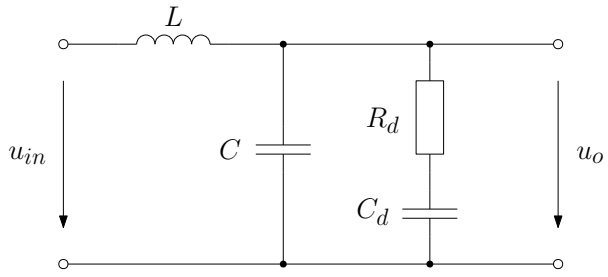

Figure 3.5.: EMI filter with RC damping network

In Fig. 3.5, an EMI input filter with RC damping network is shown. The transfer function of an LC low-pass filter with a resistive load R is described by Eq. (3.13) to (3.15). Accordingly, the cut-off frequency ω_c can be selected by Eq. (3.14). Moreover, the damping ratio d is inversely proportional to the load resistance R as visible in Eq. (3.15). For adequate damping, the load resistance must be small therefore.

$$H_{LP}(s) = \frac{\omega_c^2}{s^2 + 2d\omega_c s + \omega_c^2} \tag{3.13}$$

$$\omega_c = \frac{1}{\sqrt{LC}} \tag{3.14}$$

$$d = \frac{1}{2R}\sqrt{\frac{L}{C}} \tag{3.15}$$

Since the input impedance of a buck converter is mostly not sufficiently small and non-constant around the filter's cut-off frequency, the EMI filter must be specially damped. An RC damping network can be added in parallel with the buck converter for blocking DC current but adequately damping the filter around the resonant frequency. Therefore, the blocking capacitor C_d must be definitely larger than the filter capacitor C. In the implemented buck converter, the blocking capacitor was selected more than 2 times larger than the filter capacitor. For selecting the value of the resistance R_d optimally, equations are given in [24]. However, the losses of the filter inductor and capacitor are not considered, hence the resistance value was selected with an LTspice simulation, based on SPICE [25], for optimum damping.

The EMI filter was designed for a cut-off frequency f_c of $10kHz$, much lower than the switching frequency and 6 times lower than the cut-off frequency of the output filter. Consequently, it can be assumed with confidence that the current through inductor

L is strongly smoothed and corresponds to the averaged input current in Eq. (2.29). The averaged input current is responsible for the heat in the inductor L and the saturation current must not be selected significant higher. Accordingly, a compatible inductor can be selected. The nominal capacitor voltages should be selected higher than the input voltage with an extra safety margin for a small voltage ripple. Finally, the requisite ripple current for selecting the filter capacitor C is determined from Eq. (2.29) and (3.10) by following equation.

$$I_{C_{RMS}} = \sqrt{I_{in_{RMS}}^2 - I_{in}^2} = \sqrt{D\left(I_o^2\, D' + \frac{1}{3}\,\Delta I_L^2\right)} \tag{3.16}$$

3.4. FPGA Design

An Intel Cyclone 10LP FPGA is used for controlling the high- and low-side FETs of the half-bridge. In the Intel Cyclone 10LP FPGA, more precisely the 10$CL025YU256I7G$ device, 25k logic elements (LEs), 66 9$kbit$ SRAM memory blocks, 66 18$bit \times 18bit$ multipliers and 4 phase-locked loops (PLLs), optimized for low cost and low power are integrated in a 256-pin FineLine BGA package of size $14mm \times 14mm$. For simplicity, the Cyclone 10LP FPGA was employed on the standard evaluation kit from Intel.

The PWM signals and the dead times for the high- and low-side FETs of the half-bridge are generated by a counter running at an internal clock frequency of 200MHz. When the button $PB0$ is pressed on the evaluation board, the counter starts counting. The signals for the high- and low-side FET are now switched on or off according to the duty cycle threshold, whereby the two FETs are never switched on simultaneously. A dead time of 10ns is inserted between switching the two FETs to avoid them shorting and destroying the power stage. Consequently, a switched PWM signal with adjustable duty cycle and 1MHz switching frequency is generated by the half-bridge.

The FPGA design was done with the High-Level Synthesis (HLS) Compiler from Intel. A HLS tool, such as the Intel HLS Compiler, transforms untimed functional code into a timed register-transfer level (RTL) implementation. High-level synthesis is thus a promising way to enhance productivity by means of abstraction [26].

4. Measurements and Verification

In this chapter, the investigations of buck converters for driving high-power laser diodes are performed on an actual implementation of a DBR tapered laser diode [3]. The considerations and insights obtained in chapter 2 are analyzed further and compared against the measurements. Therefore, measurements of the dynamic transient responses of the laser current are conducted and verified by the step responses of the modeled transfer functions. Moreover, the filtering characteristics of the 1^{st}, 2^{nd} and 3^{rd} order output filters of a buck converter are analyzed and compared.

As the high-power laser diode is modeled electrically by a resistor at the operation point in chapter 2, the dynamic modeling will be verified first on a buck converter with a resistive load. Subsequently, a buck converter driving the tapered section of a high-power DBR tapered laser diode [3] will be analyzed.

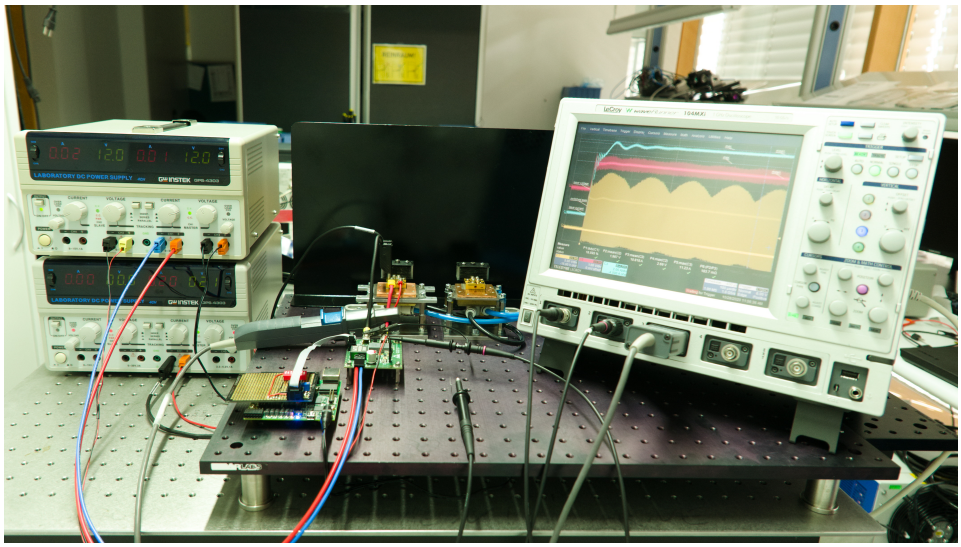

Figure 4.1.: Picture of the measurement setup in the laser laboratory

In Fig. 4.1, the general measurement setup of the buck converter driving the tapered section of a 8W DBR tapered laser diode is shown. The tapered section of the DBR tapered laser diode is driven by the buck converter (designed in Ch. 3) and the ridge waveguide section by a constant current source (bottom power supply) at the

operation point of $200mA$. The buck converter is supplied by constant voltages of $12V$ (top power supply). To generate the PWM signal for the GaN half-bridge of the buck converter, an Intel Cyclone 10LP FPGA evaluation board is used. All measurements are done by a 4-channel $10GS/s$ LeCroy WaveRunner 104MXi oscilloscope and for current measurements a LeCroy $AP015$ current probe is moreover applied. To keep the temperature of the high-power laser diode constant at $25°C$ a water cooling system is employed. More details on the measurement setup are found in Appendix B.

4.1. Buck Converter with a Resistive Load

For comparison and verification of the modeling results of chapter 2, measurements are performed on a buck converter with a resistive load. Therefore, the DBR tapered laser diode in Fig. 4.1 is replaced by a common $5W$ wirewound resistor of $100m\Omega$.

First of all, the dynamic transient responses of the output current are measured, which are compared and verified by the step responses of the modeled control-to-output transfer functions. Thereafter, measurements of the output current ripple are performed and the filtering characteristics of the output filters are discussed.

4.1.1. Dynamic Transient Responses

The dynamic transient responses are measured by abruptly switching on the pulse-width modulation control signals of the GaN half-bridge, which are generated by the FPGA when a button is pressed on the evaluation board. As a result, the output voltage of the buck converter rises and causes a proportional current in the resistive load. For accurate measurements of the voltage and current transient responses, the oscilloscope is triggered to the first rising edge of the amplified PWM signal at the switched output of the half-bridge.

In Fig. 4.2, the measured output voltage and current transient responses of a buck converter with a resistive load of $100m\Omega$ are shown. When the PWM signal at the output of the GaN half-bridge is switched on, the output current rises proportional to the output voltage of the buck converter. As shown in Fig. 4.2 the output voltage is disturbed by short periodical voltage peaks. These peaks are synchronous to the switched output signal of the GaN half-bridge, which indicates the voltage peaks are caused by electromagnetic interferences. By the comparison in Fig. 4.3 it is clear that the voltage spikes are more precisely caused by fast switching of the PWM pulses and by their transient oscillations. However, as the spikes are not detectable in the output current, it is obvious that they are induced by measuring the output voltage.

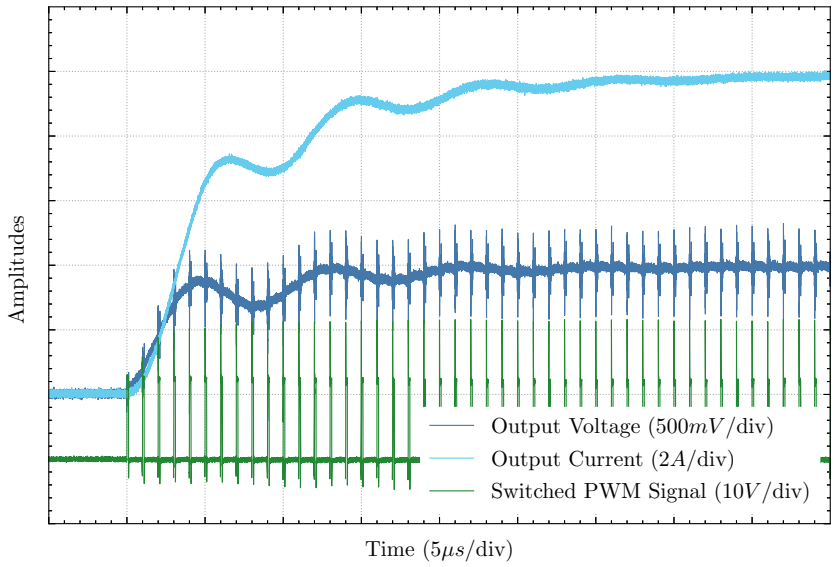

Figure 4.2.: Oscilloscope like representation of the measured transient responses: The PWM signal is abruptly switched on and amplified by the GaN half-bridge, the output voltage of the buck converter rises and results in an output current in the resistive load of 100$m\Omega$

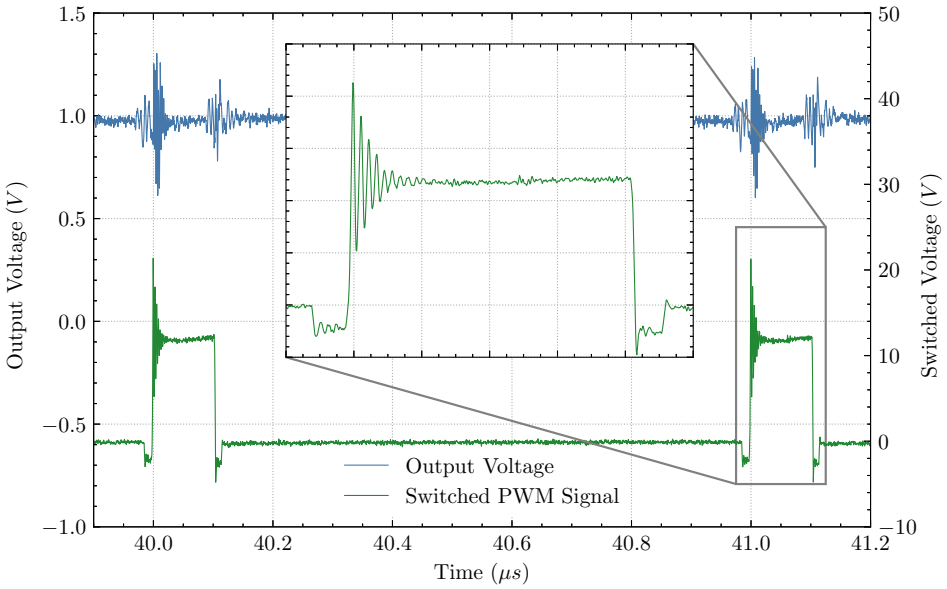

Figure 4.3.: Comparison of the measured output voltage and the switched PWM signal at the output of the GaN half-bridge: The switched PWM signal is generated with a switching frequency of 1MHz and a duty cycle of 10.4%, the spikes of the output voltage are caused by fast switching of the PWM pulses and by their transient oscillations

As seen in the picture of Fig. 4.1, the interferences are probably coupled in by the long mass wire of the second probe. Consequently, the disturbances could be reduced by enhanced voltage measurements or by an improved measuring setup. However, since voltage measurement is not as important as current measurement in this application, no additional effort is made.

To verify the modeling results, the measured transient responses are now compared to the step responses of the modeled control-to-output transfer functions. Therefore, the output current transient responses are measured at various duty cycles D, when the amplified PWM signal at the output of the half-bridge is abruptly switched on. The measured transient responses are subsequently compared to the scaled step responses of the corresponding output current to duty cycle transfer functions.

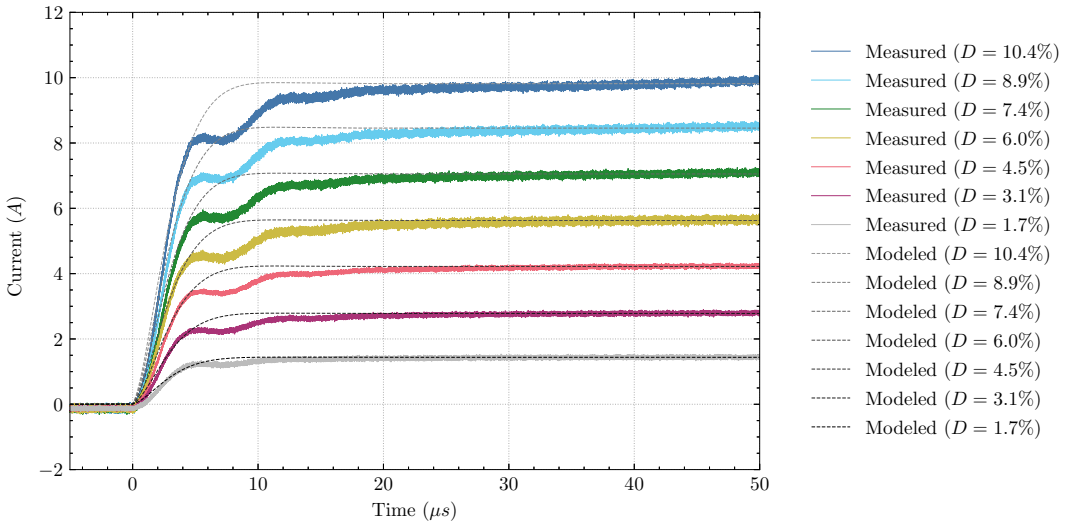

Figure 4.4.: Comparison of the measured (solid lines) and modeled (dashed lines) transient responses: When the PWM signal is abruptly switched on at various duty cycles D, an output current is generated by the conventional buck converter 2^{nd} order on a resistive load of $100m\Omega$, which is compared to the step response of the modeled control-to-output transfer function

In Fig. 4.4, the measured and modeled transient responses of the output currents generated by a conventional buck converter 2^{nd} order are shown. For these measurements, the inductance L_2 of the output filter of the implemented buck converter was replaced by a wire in the circuit. The modeled transient responses are determined by calculating the step response of the output current to duty cycle transfer function in Eq. (2.130) with Python [27] numerically and by scaling to the amplitudes of the measured transient responses. As a result, the measured and modeled transient responses can now be compared.
As shown in Fig. 4.4, the modeled transient responses are not matching exactly to the measured transient responses of the output currents. The slopes of the curves are similar, but an additional bend occurs in the measured output currents. Experi-

mentally, the inductance of the connection wires to the load is added to the model. For modeling the output current to duty cycle transfer function of the higher order buck converter in Eq. (2.142) can be used. Thus, the modeled transient responses including the wire inductance are determined from the transfer function in Eq. (2.142). In Fig. 4.5 the modeled transient responses with an experimentally established wire inductance of $180nH$ are shown. As illustrated, the modeled transient responses now correspond to the measured output currents. Consequently, the wire inductance should be considered in modeling.

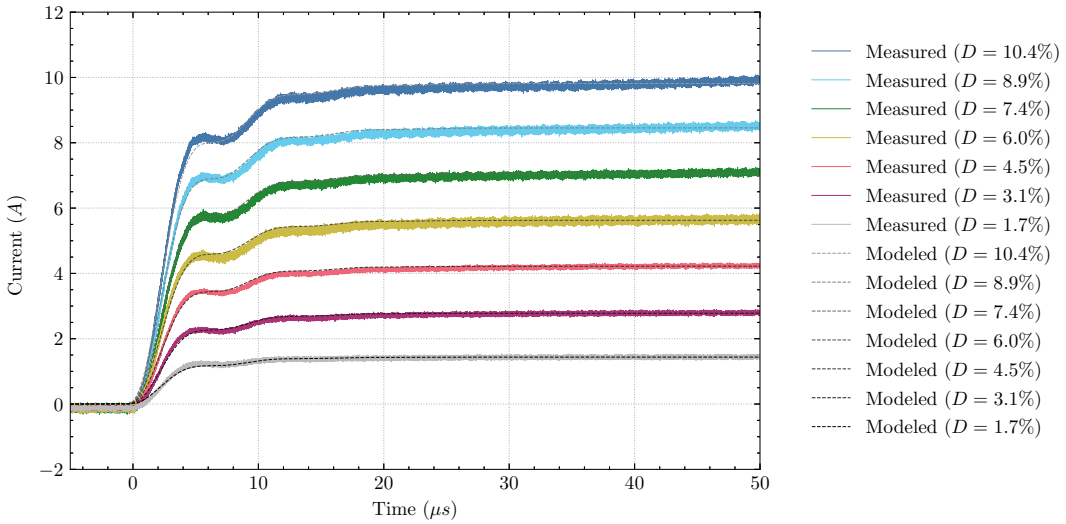

Figure 4.5.: Comparison of the measured (solid lines) and modeled (dashed lines) transient responses: When the PWM signal is abruptly switched on at various duty cycles D, an output current is generated by the conventional buck converter 2^{nd} order on a resistive load of $100m\Omega$ with included wire inductance of $180nH$, which is compared to the step response of the modeled control-to-output transfer function

The measured and modeled transient responses of an extended buck converter 3^{rd} order are compared next. The output currents are therefore measured directly on the implemented buck converter with a resistive load of $100m\Omega$. Modeling is performed by calculating and scaling the step response of the output current to duty cycle transfer function of the higher order buck converter in Eq. (2.142). Thereby, the wire inductance can be simply added to the output inductor of the filter. The comparison of the measured and modeled transient responses of the buck converter 3^{rd} order driving a resistive load of $100m\Omega$ with $180nH$ wire inductance is shown in Fig. 4.6. It is clearly visible that the modeled transient responses are matching well with the measured output currents.

Finally, the comparison of the measured and modeled transient responses of a reduced buck converter 1^{st} order is performed. For the measurements, the inductance L_2 of the output filter of the implemented buck converter was replaced by a wire and

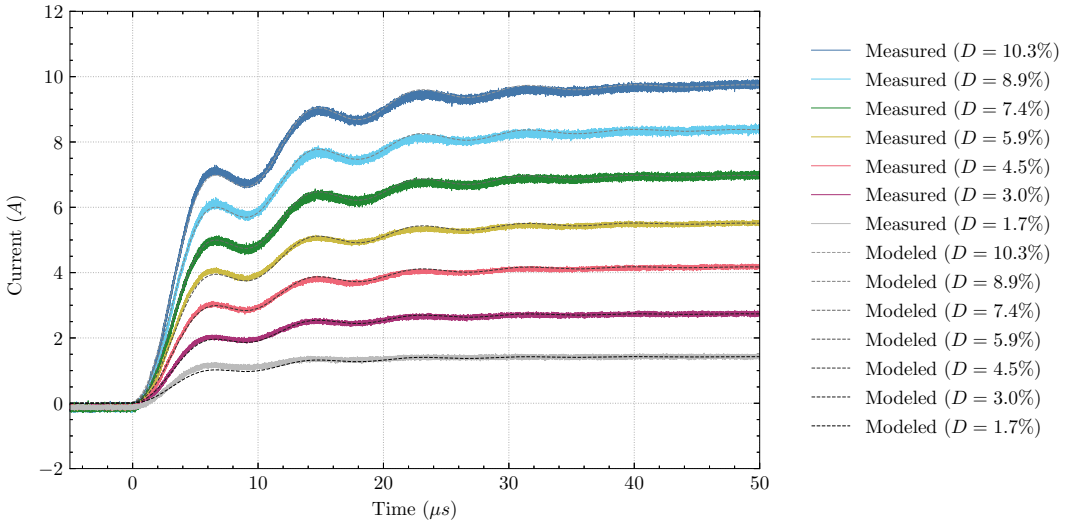

Figure 4.6.: Comparison of the measured (solid lines) and modeled (dashed lines) transient responses: When the PWM signal is abruptly switched on at various duty cycles D, an output current is generated by the extended buck converter 3^{rd} order on a resistive load of $100m\Omega$ with included wire inductance of $180nH$, which is compared to the step response of the modeled control-to-output transfer function

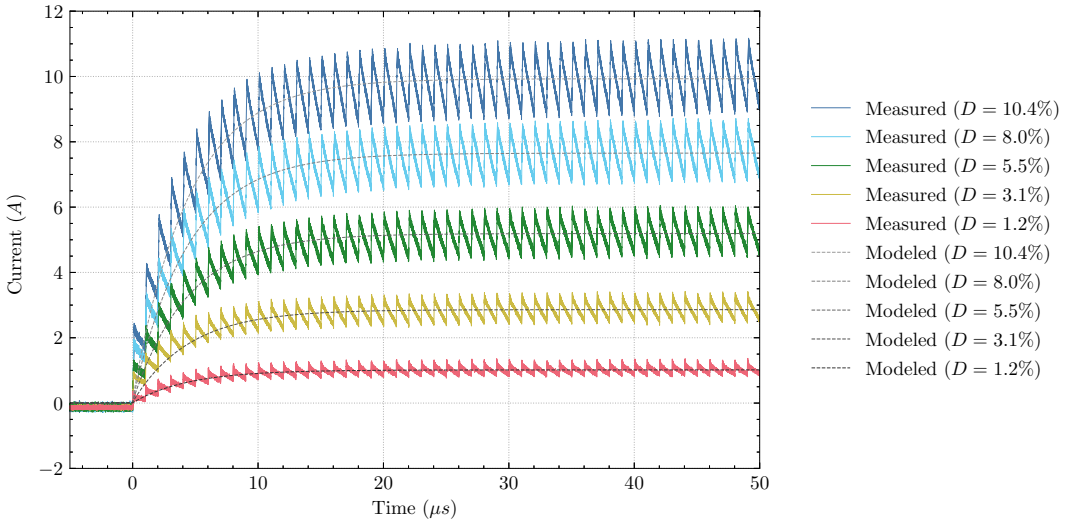

Figure 4.7.: Comparison of the measured (solid lines) and modeled (dashed lines) transient responses: When the PWM signal is abruptly switched on at various duty cycles D, an output current is generated by the reduced buck converter 1^{st} order on a resistive load of $100m\Omega$ with included wire inductance of $180nH$, which is compared to the step response of the modeled control-to-output transfer function

additionally the filter capacitor C_1 was removed. The modeled transient responses are determined from the step responses of the reduced transfer function in Eq. (2.133). For considering wire inductance, the additional inductance was added to the value of the inductor L in the transfer function. The measured and modeled transient responses of the reduced buck converter 1^{st} order are shown in Fig. 4.7. It is visible that the modeled step responses correspond to the slopes of the measured output currents on average. However, the ripple of the output currents are not taken into account. The ripple of the output currents are examined separately in the next section.

In summary, the transient response of a buck converter 1^{st}, 2^{nd} and 3^{rd} order can be modeled accurately on a resistive load, if the inductance of the connecting wires is included. As the inductance of the load's connecting wires is actually always present, the additional inductance must be considered. On a 1^{st} and 3^{rd} order output filter the filtering order remains unchanged and the connecting wire inductance can simply be added to the output inductor. In a conventional buck converter 2^{nd} order, the inductance of the connecting wires increases the filtering order, which practically always results in a buck converter 3^{rd} order.

4.1.2. Output Ripple Current

The measurements of the output current ripple are now treated in detail and the filtering characteristics of the output filters of the buck converters are analyzed.
The ripple of the output currents on a buck converter are measured in steady-state, after more than $1ms$ when a button was pressed on the evaluation board. In steady-state the output voltage and current of a buck converter are stable and constant in average. For measuring the small current ripple, the DC component of the signal is removed by AC coupling in the oscilloscope.

In Fig. 4.8, the measured AC coupled voltage and current output ripple of a buck converter 3^{rd} order with a resistive load of $100m\Omega$ and included wire inductance of $180nH$ are shown. The switched PWM signal with duty cycle $D = 6\%$ generated by the GaN half-bridge is measured and contrasted. As shown in Fig. 4.8, the current output ripple is synchronous to the switching frequency of the PWM signal. More precisely, one period of the current ripple occurs exactly in one switching period of the PWM signal.
For analyzing the ripple waveforms of the buck converters 1^{st}, 2^{nd*} and 3^{rd} order, the ripple of the output currents, measured with AC coupling, are shown in Fig. 4.9. As discussed previously, the inductance of the load's connecting wires must be considered. With an output filter 1^{st} order, the additional inductance is added to the output inductor, which does not affect the filtering order. Over the cut-off frequency a

*It is practical a filter 3^{rd} order, as inductance of the load's connecting wires must be considered

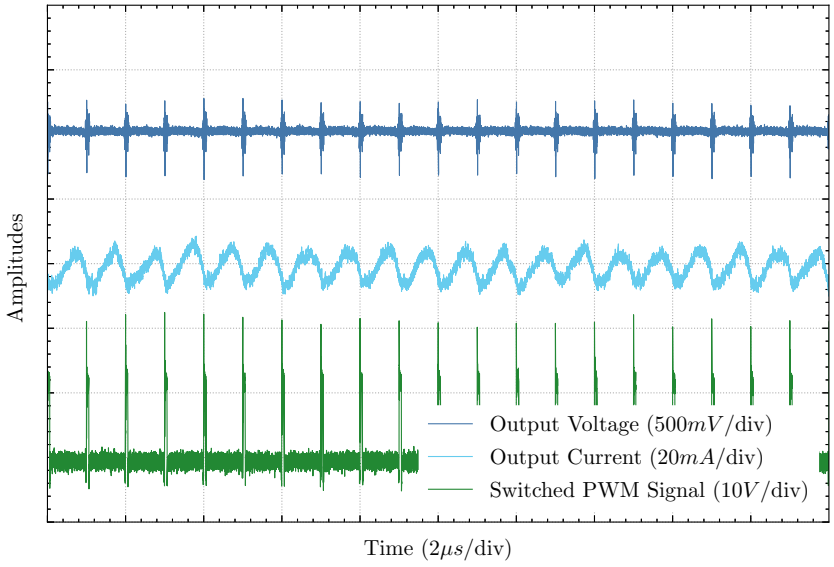

Figure 4.8.: Oscilloscope like representation of the measured voltage and current output ripple: In steady-state the output voltage and current are measured (AC coupled) on a buck converter 3^{rd} order with a resistive load of $100m\Omega$ and are contrasted to the measured (DC coupled) switched PWM signal with duty cycle $D = 6\%$ at the output of the GaN half-bridge

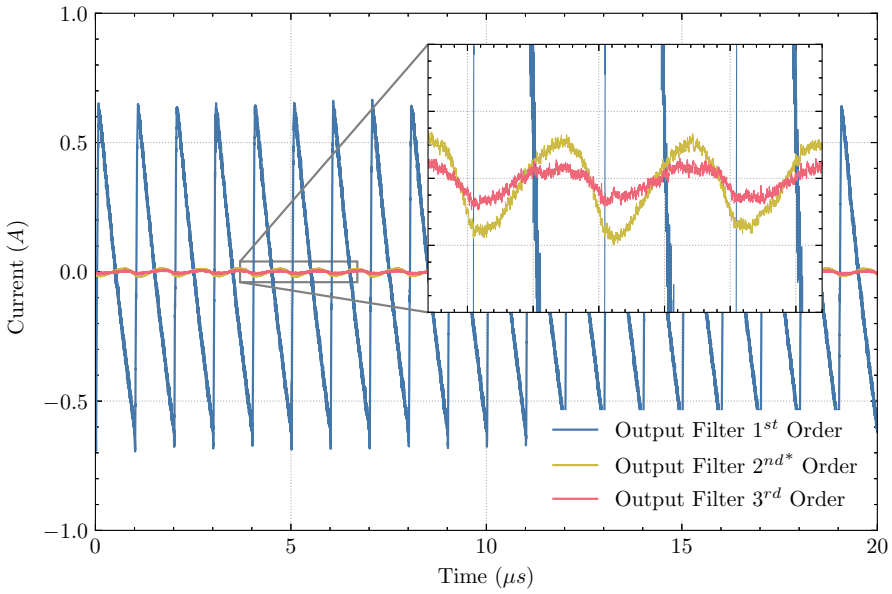

Figure 4.9.: Comparison of the ripple waveforms of the measured output currents: In steady-state the output currents of the buck converters 1^{st}, 2^{nd*}, 3^{rd} order with included wire inductance of $180nH$ and a resistive load of $100m\Omega$ are measured (AC coupled) and compared for a duty cycle D of 6%

low-pass filter 1^{st} order has integrating properties, which results in a large triangular current ripple as shown in Fig. 4.9. On a 2^{nd} order filter, the inductance of the connecting wires increases the filtering order to a 3^{rd} order. Consequently, by integrating the switched PWM signal three times, the current ripple becomes sinusoidal. Otherwise, by increasing the filter order the harmonics are more attenuated, which causes the output signal to become more and more sinusoidal. Accordingly, the current ripple on a 2^{nd*} order buck converter with $180nH$ wire inductance is reduced significantly. By increasing the filter to a 3^{rd} order, the wire inductance is simply added to the output inductor, resulting in a filter 3^{rd} order again. Consequently, the current ripple in Fig. 4.9 is damped further.

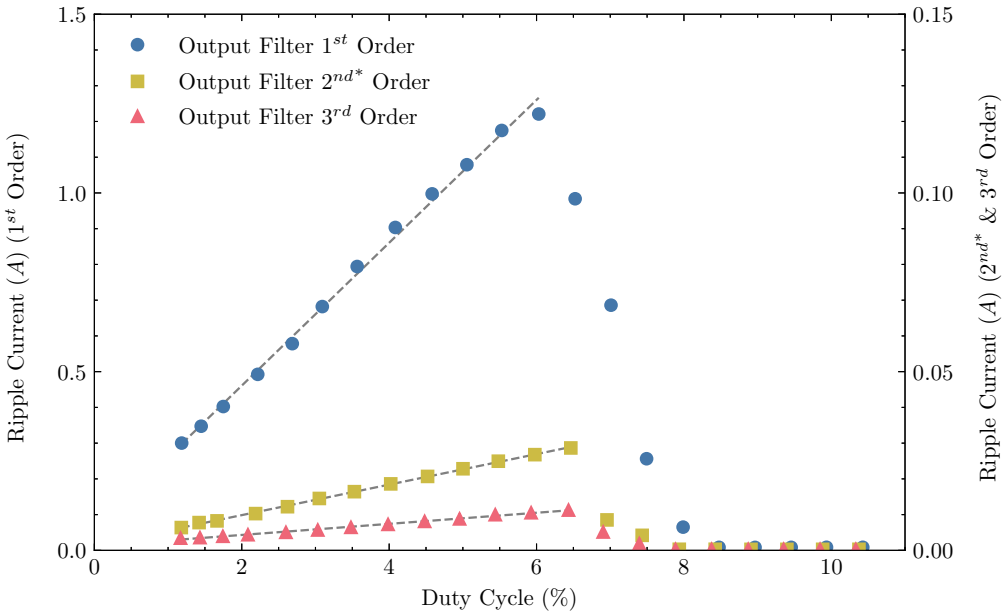

Figure 4.10.: Comparison of the ripple amplitudes of the measured output currents: In steady-state the peak-to-peak ripple amplitudes of the output currents are measured at various duty cycles on buck converters with a resistive load of $100m\Omega$ and included wire inductance of $180nH$, which are compared for the output filters 1^{st}, 2^{nd*}, 3^{rd} order

The attenuation of the current ripple of the 1^{st}, 2^{nd*} and 3^{rd} order output filters are compared now. Therefore, the current ripple amplitudes, more precisely the peak-to-peak amplitudes are measured at increasing values of the duty cycles on a buck converters with a resistive load and $180nH$ wire inductance. The measured peak-to-peak amplitudes of the output ripple currents are shown in Fig. 4.10. Note that for comparison the measured amplitudes of the 1^{st} order output filter are scaled to the left and the amplitudes of the 2^{nd*} and 3^{rd} order output filters to the right axes. For duty cycles lower than 6%, the ripple amplitudes rise linearly, thereafter the amplitudes are falling to zero. It does not make any sense, that the output current

*It is practical a filter 3^{rd} order, as inductance of the load's connecting wires must be considered

ripple of a buck converter disappears for high duty cycle values. Therefore, it is more obvious that the amplitude drop is caused by a dramatically reduced sensibility of the AP015 current probe for higher output currents. Thus, these values should not be taken into account. For duty cycles lower than 6%, the ripple amplitudes rise linearly by the duty cycles. As the switched PWM signal is smoothed by the output filter, an output voltage proportional to the duty cycle is generated by the buck converter, which results in a proportional output current on a resistive load. Consequently, the ripple amplitudes rise proportional respectively linear to the duty cycles. The comparison in Fig. 4.10 illustrates, that the ripple amplitudes of the 2^{nd*} and 3^{rd} order output filters are much smaller than the 1^{st} order. Moreover, the gradient of the ripple amplitudes is reduced by increasing the output inductor or the wire inductance. As a result, buck converters 2^{nd*} and 3^{rd} order with included wire inductance are significantly better for filtering the output current.

4.2. Buck Converter driving a High-Power Laser Diode

The investigations of buck converters for driving the tapered section of a high-power DBR tapered laser diode [3] are presented now. Like before, the dynamic transient responses of the output current are measured and compared to the step responses of the modeled control-to-output transfer functions. Moreover, measurements of the output current ripple are performed and the filtering characteristics of the output filters 1^{st}, 2^{nd} and 3^{rd} order are analyzed and contrasted to the buck converter with a resistive load.

Typically, a laser diode is described electrically by the current-voltage characteristic curve. The static characteristic curve is generally measured in steady-state, where the voltage and current do not change. For measuring the current-voltage characteristic curve of the tapered section of the DBR tapered laser diode, the laser diode is driven now by a buck converter. The voltages and currents on the laser diode are measured thereby for increasing duty cycles in steady-state and are plotted as shown in Fig. 4.11. The load, which presents the laser diode at the output of a buck converter, is determined by applying the Ohm's law to the measured values.
As shown in Fig. 4.11, no current flows through the laser diode for output voltages lower than $1.2V$. For higher voltages the current rises, until it increases approximately linear to the output voltage. Furthermore, the resistance of the diode is highly resistive for lower voltages. For voltages higher than $1.2V$ the resistance drops strongly and becomes low-ohmic. As a result, the laser diode is absolutely non-linear as a load.

*It is practical a filter 3^{rd} order, as inductance of the load's connecting wires must be considered

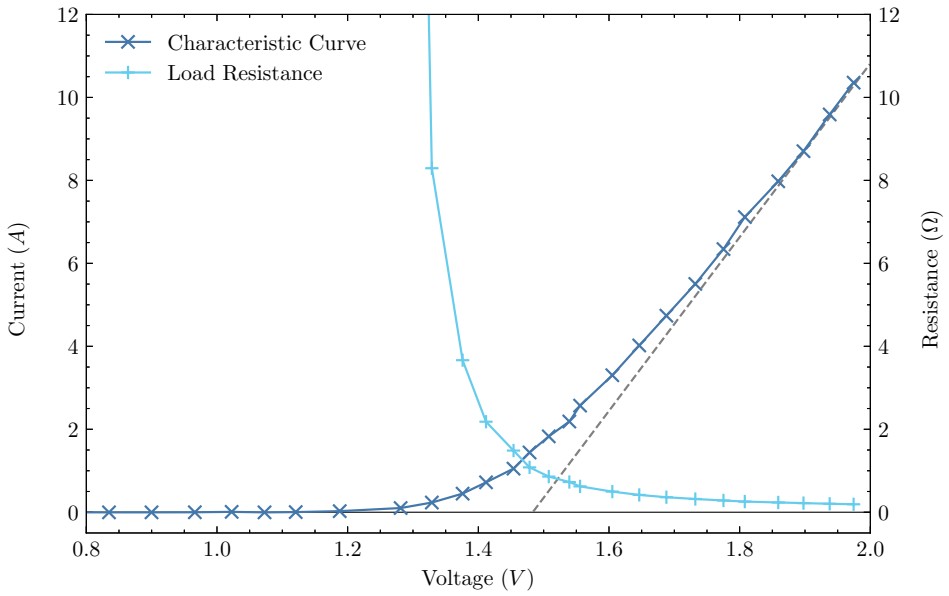

Figure 4.11.: Measured characteristic curve and load resistance of the DBR tapered laser diode: The current-voltage characteristic curve of the tapered section of the DBR tapered laser diode, driven by a buck converter is measured in steady-state and the load resistance of the laser diode is determined by applying the Ohm's law

4.2.1. Dynamic Transient Responses

The dynamic transient responses are measured in the same manner as for the buck converter with a resistive load. By abruptly switching on the PWM signal amplified by the GaN half-bridge, the output voltage of the buck converter rises and results in an output current in the DBR tapered laser diode. For measuring the transient responses of the output voltage and current, the oscilloscope is triggered to the first rising edge of the switched PWM signal.

In Fig. 4.12, the measured transient responses of a buck converter driving the tapered section of the DBR tapered laser diode are shown. As visible, the output voltage rises immediately when switching on the switched PWM signal. However, the output current is delayed, since the current through the laser diode only occurs when the output voltage exceeds $1.2V$ as shown in Fig. 4.11.
The measured transient responses are compared now to the step responses of the modeled control-to-output transfer functions. Therefore, the output current transient responses are measured at various duty cycles D, when the amplified PWM signal at the output of the half-bridge is abruptly switched on. The measured transient responses are subsequently compared to the scaled step responses of the corresponding output current to duty cycle transfer functions at the operation points.

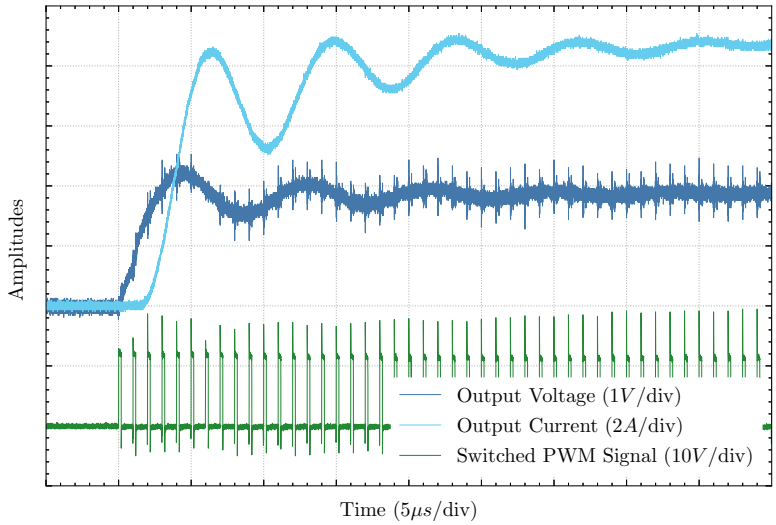

Figure 4.12.: Oscilloscope like representation of the measured transient responses: The PWM signal is abruptly switched on and amplified by the GaN half-bridge, the output voltage of the buck converter rises and results in an output current in the DBR tapered laser diode

In Fig. 4.13, the measured and modeled transient responses of the output currents generated by a conventional buck converter 2^{nd} order are shown. For the measurements, the inductance L_2 of the output filter of the implemented buck converter was replaced by a wire in the circuit. The modeled transient responses are determined by calculating numerically the step responses of the output current to duty cycle transfer function in Eq. (2.130) for the load resistances of Fig. 4.11 at the operation points and by scaling to the amplitudes of the measured transient responses. As a result, the measured and modeled transient responses are comparable.
As illustrated in Fig. 4.13, the modeled transient responses are not matching to the measured transient responses of the output currents. High frequency oscillations occur at the beginning of the transient responses, which are caused by the 2^{nd} order output filter. Thereafter, the output currents increase further and another low frequency oscillation arises. First of all, the low frequency oscillation is examined more closely. In Fig. 4.14, the measured output current transient responses of the 2^{nd} and 3^{rd} order buck converter are compared. As shown, the order of the output filter does not affect the oscillation frequency. Moreover, the low frequency oscillations occur for buck converters driving a DBR tapered laser diode or a resistive load. Consequently, the oscillations are not caused by the output filter or by the load. However, the oscillation frequency can be determined by a oscillation period. As visible in Fig. 4.14, the oscillation period is approximately $100\mu s$, which results in an oscillation frequency of $10kHz$. The frequency is close to the cut-off frequency of the EMI-filter, hence it is assumed that the oscillations are caused by the EMI-filter. A LTspice simulation, based on SPICE [25], proved that they are caused by the EMI-filter. The EMI-filter is damped at the cut-off frequency, but not as much as intended. The damping of the filter could be improved further if needed.

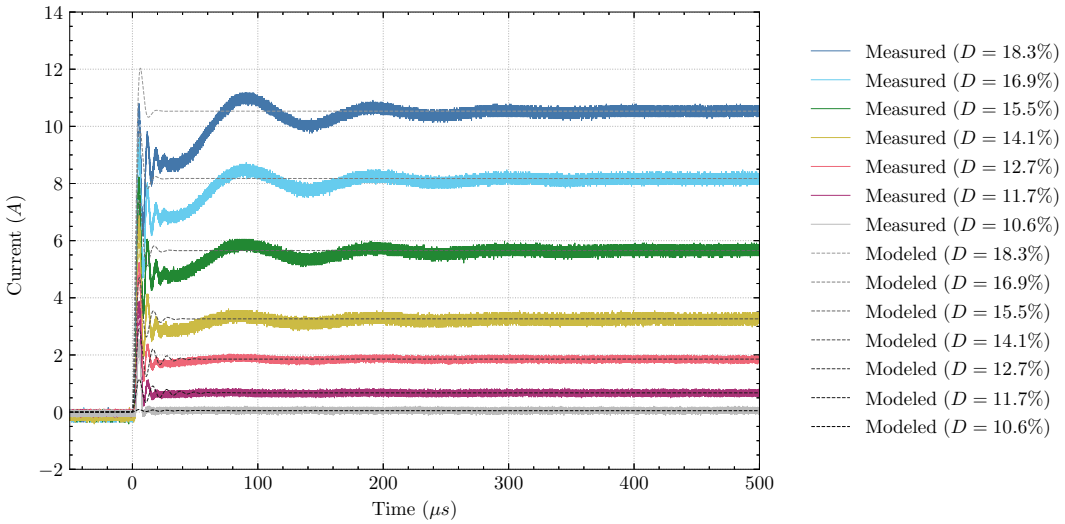

Figure 4.13.: Comparison of the measured (solid lines) and modeled (dashed lines) transient responses: When the PWM signal is abruptly switched on at various duty cycles D, an output current is generated by the conventional buck converter 2^{nd} order on the DBR tapered laser diode, which is compared to the step response of the modeled control-to-output transfer function at the operation points

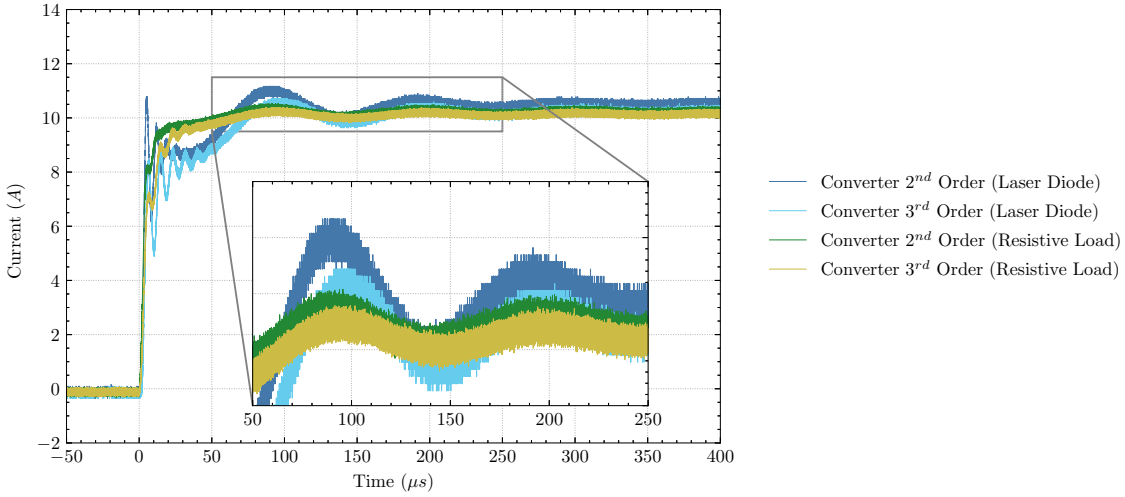

Figure 4.14.: Comparison of the low frequency oscillations of the transient responses: The measured output current transient responses of the 2^{nd} and 3^{rd} order buck converters with resistive and DBR tapered laser diode load are compared for analyzing the low frequency oscillations

The high frequency oscillations occurring at the beginning of the transient responses are analyzed next. In Fig. 4.15, a more detailed illustration of the measured and modeled transient responses of a conventional buck converter 2^{nd} order in Fig. 4.13 is shown. The modeled transient responses increase earlier, but less steeply than the measured ones. The oscillation does not occur at the same position and subsides more quickly. Moreover, the oscillation subsides less rapidly for small duty cycles than for large, which happens in the opposite way for the measured transients. All in all, the modeled and measured transient responses are not matching.

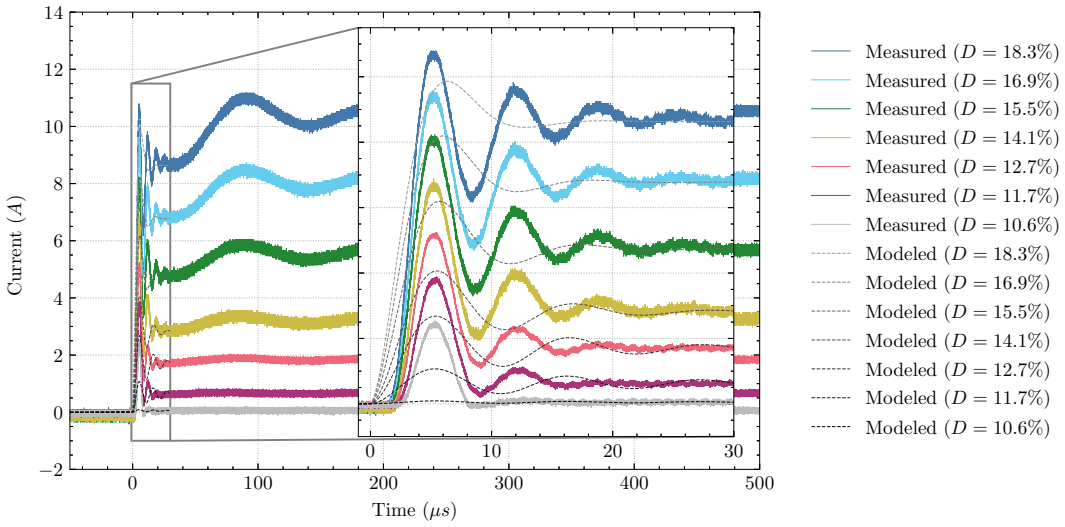

Figure 4.15.: Comparison of the measured (solid lines) and modeled (dashed lines) transient responses: When the PWM signal is abruptly switched on at various duty cycles D, an output current is generated by the conventional buck converter 2^{nd} order on the DBR tapered laser diode, which is compared to the step response of the modeled control-to-output transfer function at the operation points (detailed illustration)

As for the buck converter with a resistive load, the inductance of the load's connection wires is now experimentally taken into account. Therefore, the modeled transient responses including the wire inductance are determined from the transfer function of the higher order buck converter in Eq. (2.142). In Fig. 4.16, the modeled transient responses with an experimentally determined wire inductance of $300nH$ are shown. As illustrated, the modeled oscillations subside less rapidly than in Fig. 4.15, but still do not correspond to the measured output currents. A more appropriate value for the wire inductance could not be found.

The measured and modeled transient responses of the extended buck converter 3^{rd} order are compared next. The output currents are measured directly on the implemented buck converter without modification. Modeling is performed by calculating the step response of the output current to duty cycle transfer function of the higher order buck converter in Eq. (2.142) for the load resistances at the operation points.

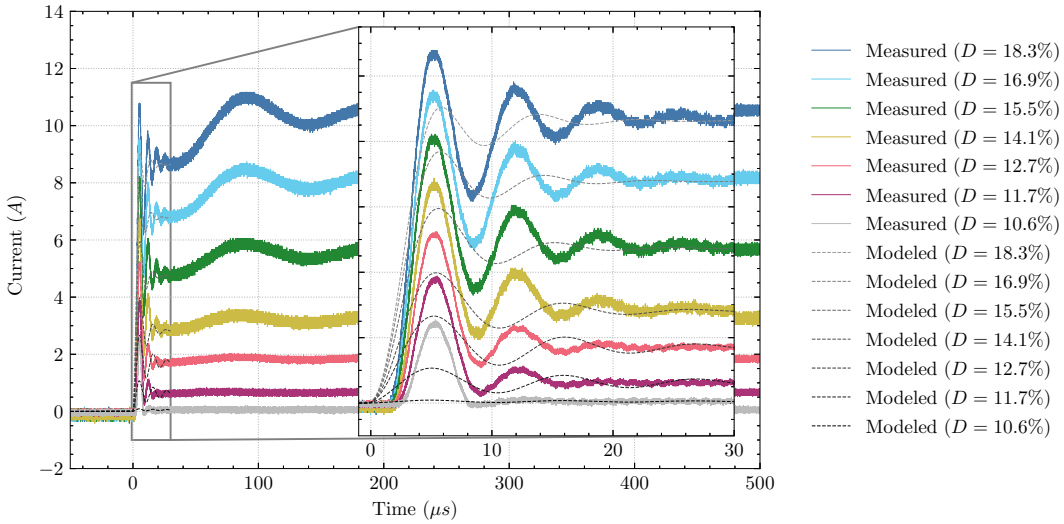

Figure 4.16.: Comparison of the measured (solid lines) and modeled (dashed lines) transient responses: When the PWM signal is abruptly switched on at various duty cycles D, an output current is generated by the conventional buck converter 2^{nd} order on the DBR tapered laser diode with included wire inductance of $300nH$, which is compared to the step response of the modeled control-to-output transfer function at the operation points

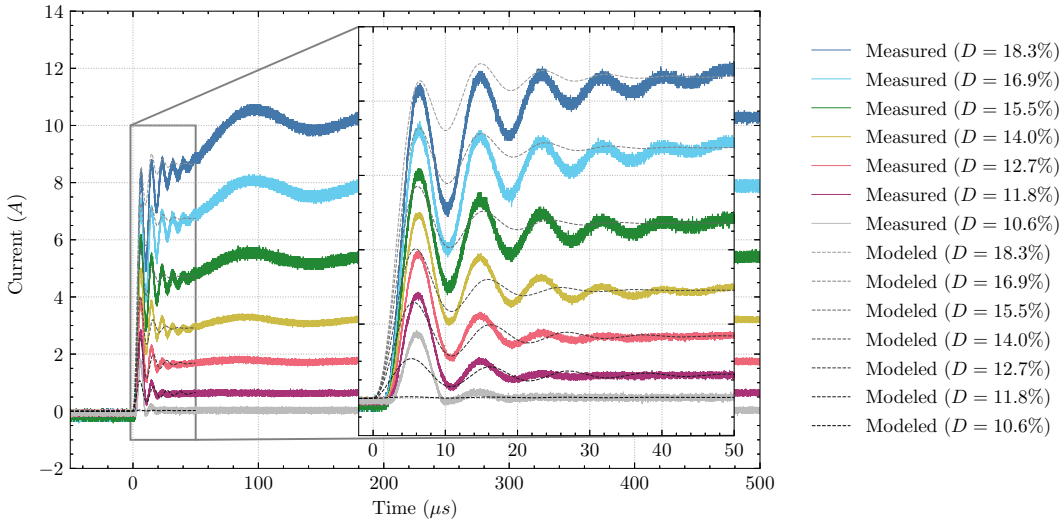

Figure 4.17.: Comparison of the measured (solid lines) and modeled (dashed lines) transient responses: When the PWM signal is abruptly switched on at various duty cycles D, an output current is generated by the extended buck converter 3^{rd} order on the DBR tapered laser diode with included wire inductance of $180nH$, which is compared to the step response of the modeled control-to-output transfer function at the operation points

Therefore, the wire inductance is simply added to the output inductor of the filter. A comparison of the measured and modeled transient responses of the buck converter 3^{rd} order driving the tapered section of the DBR tapered laser diode with included $180nH$ wire inductance is shown in Fig. 4.17. At first glance, it seems that the modeled and measured oscillations correspond partly. However, on closer observation it is clearly visible that they do not match here either.

Finally, the comparison of the measured and modeled transient responses of a reduced buck converter 1^{st} order is performed. For the measurements, the inductance L_2 of the output filter of the implemented buck converter was replaced by a wire and additionally the filter capacitor C_1 was removed. The modeled transient responses are determined from the step responses of the reduced transfer functions in Eq. (2.133) for the load resistances at the operation points. To consider the wire inductance, the additional inductance of $900nH$ was added to the inductor L in the transfer function. The measured and modeled transient responses of the reduced buck converter 1^{st} order are shown in Fig. 4.18. Interestingly, the modeled transient responses correspond to the slopes of the measured output currents on average. The slope of the modeled and measured curves match accurately for a duty cycle of 18.6%, but not for other values. Consequently, the non-linear load of the laser diode can be partially compensated by the additional inductance at some operation points.

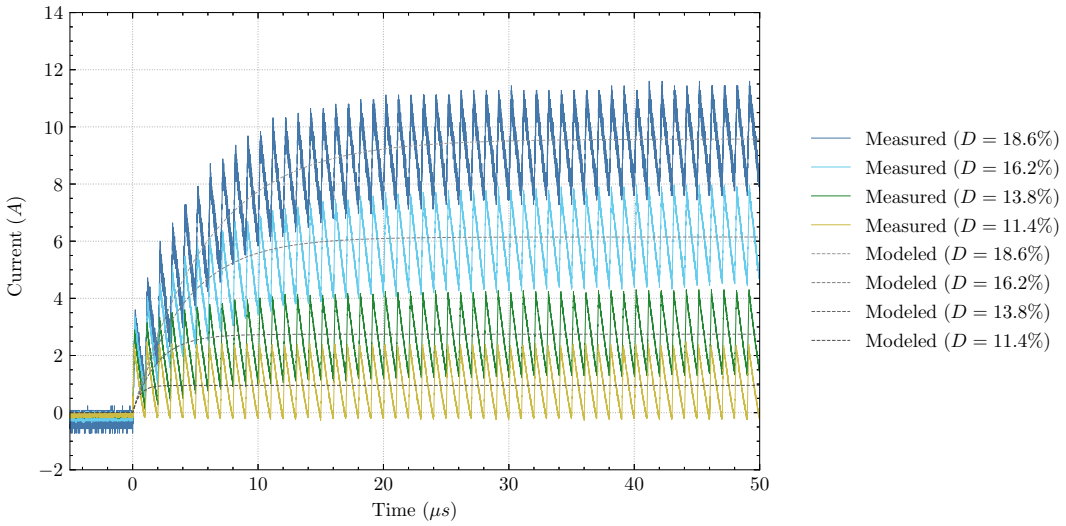

Figure 4.18.: Comparison of the measured (solid lines) and modeled (dashed lines) transient responses: When the PWM signal is abruptly switched on at various duty cycles D, an output current is generated by the reduced buck converter 1^{st} order on the DBR tapered laser diode with included wire inductance of $900nH$, which is compared to the step response of the modeled control-to-output transfer function at the operation points

Overall, the transient response of a buck converter 2^{nd} and 3^{rd} order cannot be modeled by the load resistance of the static characteristic curve at the operation point operating in continuous conduction mode. The DBR tapered laser diode is such non-linear as a buck converters load that load resistance can not be approximated by the static resistance at the operation point. As the output voltage increases, the resistance of the high-power laser diode changes from very high to low resistance as shown in Fig. 4.11. At high load resistances, a buck converter is operation in continuous conduction mode and switches to discontinuous conduction mode at low values. Accordingly, the transient responses of a buck converter driving a high-power laser diode is hard to predict and even harder to model.
Interestingly, with a 1^{st} order buck converter, the non-linear load of the laser diode can be partially compensated by the additional inductance at some operation points. Consequently, the transient response of a buck converter 1^{st} order driving the DBR tapered laser diode can be modeled with sufficient accuracy.

4.2.2. Output Ripple Current

The measurements of the output current ripple are performed and the filtering characteristics of the buck converters driving the tapered section of a DBR tapered laser diode are analyzed now. The ripple of the buck converters output currents are measured in steady-state, when a button was pressed on the evaluation board. For measuring the small current ripple, the DC component of the signal is removed by AC coupling in the oscilloscope.

For analyzing the ripple waveforms of the buck converters 1^{st}, 2^{nd*} and 3^{rd} order, the measured (AC coupled) ripple of the output currents are shown in Fig. 4.19. As the inductance of the load's connecting wires is always present, as shown for the buck converter with a resistive load, the additional inductance must be considered. With an output filter 1^{st} order, the additional inductance is added to the output inductor, which does not affect the filtering order. As discussed before, a low-pass filter 1^{st} order is integrating, which results in a large triangular current ripple as shown in Fig. 4.19. On a 2^{nd} order filter, the inductance of the connecting wires increases the filtering order to a 3^{rd} order. Accordingly, the current ripple on a 2^{nd*} order buck converter with wire inductance becomes sinusoidal and is reduced significantly. By increasing the filter to a 3^{rd} order, the wire inductance is added to the output inductor, resulting in a filter 3^{rd} order again. Consequently, the current ripple is damped further.

The attenuation of the current ripple of the 1^{st}, 2^{nd*} and 3^{rd} order output filters with wire inductance are compared now. At increasing values of the duty cycles the peak-to-peak current ripple amplitudes are measured on the buck converters

*It is practical a filter 3^{rd} order, as inductance of the load's connecting wires must be considered

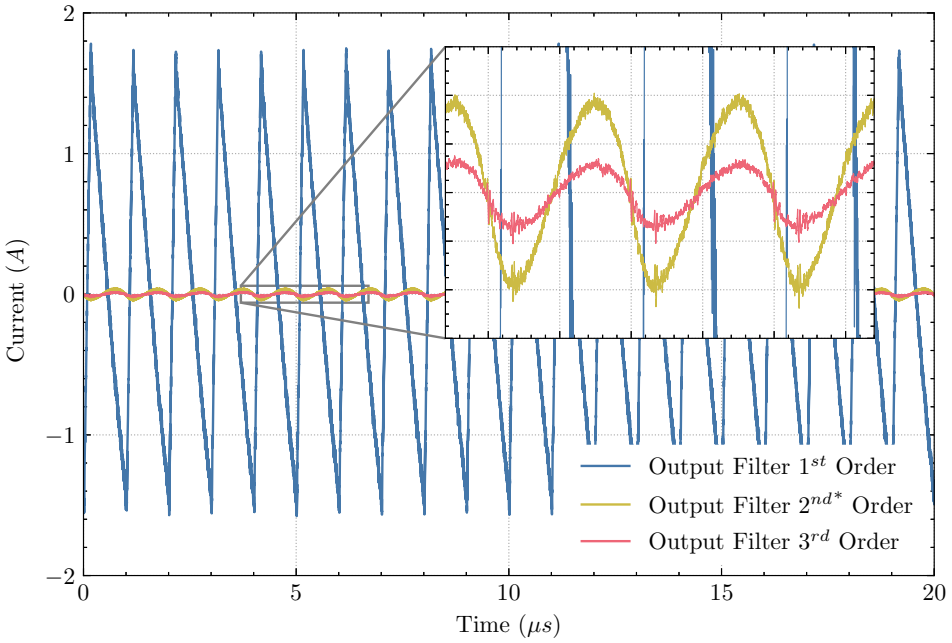

Figure 4.19.: Comparison of the ripple waveforms of the measured output currents: In steady-state the output currents of the buck converters 1^{st}, 2^{nd*}, 3^{rd} order with included wire inductance driving a DBR tapered laser diode are measured (AC coupled) and compared for a duty cycle D of 15.5%

driving the tapered section of a DBR tapered laser diode. The measured peak-to-peak amplitudes of the output ripple currents are shown in Fig. 4.20. For comparison, the measured amplitudes of the 1^{st} order output filter are scaled to the left and the amplitudes of the 2^{nd*} and 3^{rd} order output filters to the right axes. At duty cycles larger than 11%, the ripple amplitudes increase linearly. On the 2^{nd*} and 3^{rd} order buck converters, the ripple amplitudes drop to zero for duty cycles higher than 15%. As already discussed for the buck converter with a resistive load, the amplitude drop is caused by a significantly reduced sensibility of the AP015 current probe for higher output currents. Hence, these values should not be considered further. For duty cycles lower than 11%, which corresponds to an output voltage of about $1.3V$, the load resistance of the DBR tapered laser diode rises sharply as show in Fig. 4.11. Consequently, the buck converters operation changes from continuous to discontinuous conduction mode. Accordingly, the output current and current ripple of the 2^{nd*} and 3^{rd} order buck converter become zero. On the 1^{st} order buck converter, the voltage pulses in discontinuous conduction mode are still large enough to cause a current flowing through the diode. As a result, the amplitudes of these current pulses are measured with AC coupling and represented in Fig 4.20. That is way the current ripple of the 1^{st} order buck converter does not become zero.

*It is practical a filter 3^{rd} order, as inductance of the load's connecting wires must be considered

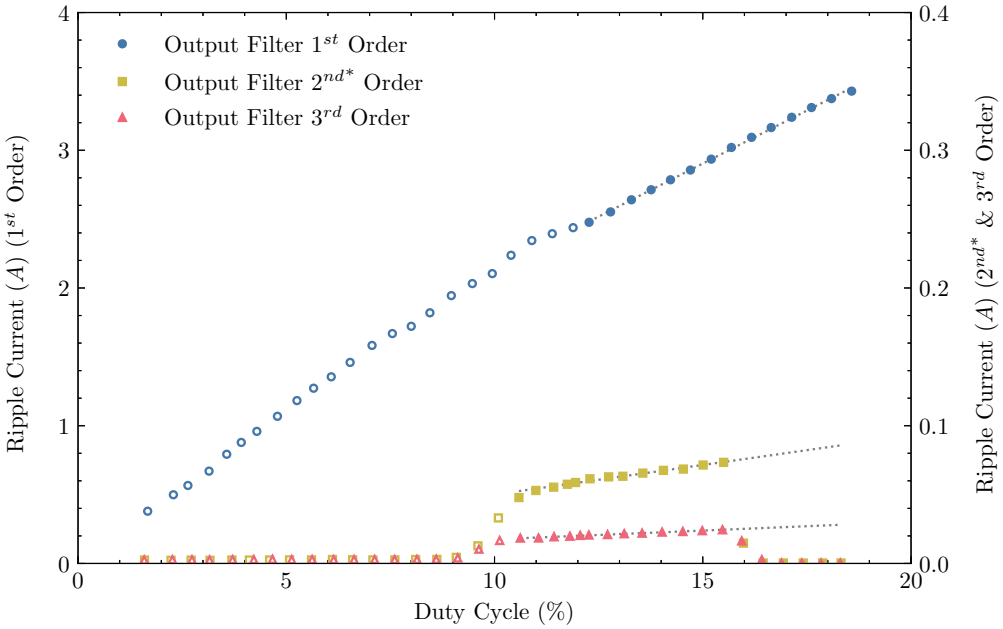

Figure 4.20.: Comparison of the ripple amplitudes of the measured output currents: In steady-state the peak-to-peak ripple amplitudes of the output currents are measured at various duty cycles on buck converters with included wire inductance driving the DBR tapered laser diode, operating in continuous (filled markers) and discontinuous (unfilled markers) conduction mode, are compared for the output filters 1^{st}, 2^{nd*}, 3^{rd} order

As illustrated in Fig. 4.20, the ripple amplitudes of the 2^{nd*} and 3^{rd} order output filters are in the linear region significantly smaller than for the 1^{st} order. Interestingly, as with the resistive load, the current ripple increases linearly for the buck converter driving a DBR tapered laser diode and is apparently little dependent on changes in diode resistance. Moreover, the gradient of the ripple amplitudes is reduced by increasing the output inductor or the wire inductance. Consequently, buck converters 2^{nd*} and 3^{rd} order with included wire inductance are significantly better for filtering the output current.

*It is practical a filter 3^{rd} order, as inductance of the load's connecting wires must be considered

5. Conclusion

The investigation of buck converters for driving high-power laser diodes was carried out by modeling the dynamics and with measurements on an actual DBR tapered laser diode. To address the stated research questions, the buck converters were modeled first using averaged state-space modeling and the two-port network theory in chapter 2. Thereafter, a 3^{rd} order buck converter was implemented in chapter 3. Measurements were performed on the tapered section of a DBR tapered laser diode [3] with an optical output power of $8W$ and the most important results are shown in chapter 4. Finally, and based on the insights obtained, an outlook of the controller design complexity is given in this chapter.

Dynamic modeling using the averaged state-space modeling approach is a natural but not straightforward procedure for modeling converters in continuous- and discontinuous conduction mode as shown in Sec. 2.2. The state-space equations of the circuit are determined separately in each switching mode, averaged over a switching cycle and are then linearized. This often results in large equations, which cannot be solved easily. In my opinion, it is convenient to additionally apply the two-port network theory for modeling more complex converters. The basic converter topologies are thus determined by the averaged state-space modeling and they are transformed or extended by the two-port network theory. Modeling of a current controlled buck converter with load effect was performed in Sec. 2.3 that way. The control-to-output and line-to-output transfer functions in Eq. (2.128) and (2.131) were thus determined analytically by a computer algebra system.
To address the research question, how suitable is a conventional buck converter for driving high currents to a power laser diode, both transfer functions were analyzed. Analyzing the line-to-output transfer function revealed that the output filter order is effectively reduced from second to first order when the load impedance of a current controlled buck converter becomes low-resistance. Accordingly, the output current ripple on a high-power laser diode should become fairly large and triangular-shaped. However, the comparison of the measured and modeled transient responses in Fig. 4.4 and 4.5 showed that the inductance of the load's connecting wires is always present and must be considered. Correspondingly, a conventional buck converter 2^{nd} order practically turns into a 3^{rd} order buck converter. Excitingly, an additional inductance was already added to the output filter of the buck converter for improving the filter characteristics during modeling in Sec. 2.4. Modeling of the higher order current controlled buck converter was accomplished there by extending the conventional

buck converter with an extra inductance using two-port network theory. From the determined line-to-output transfer function in Eq. (2.143) it is obvious that the order of the low-pass filter had increased by one compared to the conventional buck converter. Moreover, the highest order term in the transfer function does not vanish when the load impedance becomes low-resistance. Based on these results, I assumed that the buck converter 3^{rd} order would be significantly better for filtering the laser current.

A buck converter with 3^{rd} order output filter was implemented to further investigate and verify the modeling results by measurements. The buck converter was designed with an integrated GaN half-bridge from EPC and an LCL low-pass output filter, operating at a switching frequency of $1MHz$. The GaN half-bridge employed considerably simplifies the design of the buck converter, as the power FETs with included gate driver, boot-strap charging and input logic circuits are integrated within a single chip. Due to the great material properties of GaN discussed in Sec. 3.2.2, chip size is reduced significantly. The parasitic capacitances in the FET are reduced, resulting in lower switching losses and higher switching frequencies. Accordingly, the switching frequency may be selected 10 times higher than the usual $100kHz$. That results in smaller components for filtering, in lower losses and costs. Higher frequencies are challenging, however, by using appropriate components and well designed PCB, it is achievable. Moreover, an EMI filter should be designed as close as practicable to the half-bridge to reduce electromagnetic interference caused by switching input current from the buck converter as discussed in Sec. 3.3. The control signals for the half-bridge were generated by an FPGA. This is beneficial as all digital signals can be generated in an FPGA and the logic operates completely in parallel. The FPGA design was done with High-Level Synthesis, a promising way to enhance productivity by means of abstraction.

Further investigations of buck converters for driving high-power laser diodes were performed on an actual implementation of a $8W$ DBR tapered laser diode [3] as shown in Fig. 4.1. The considerations and insights obtained before were further analyzed and compared against the measurements. To verify the modeling results, measurements of the dynamic transient responses of the output currents 1^{st}, 2^{nd} and 3^{rd} order buck converters with a resistive load were compared to the step responses of the modeled control-to-output transfer functions in Sec. 4.1 first. That makes sense, as the high-power laser diode was modeled in Sec. 2.3 by a resistor at the operation point. It was shown that the transient response of a buck converter can be modeled accurately on a resistive load, if the inductance of the load's connecting wires is included as mentioned before. A 2^{nd} order buck converter turns into a 3^{rd} order converter and with 1^{st} and 3^{rd} order the connecting wires inductance can simply be added to the output inductor. The implemented buck converter driving the tapered section of a high-power DBR tapered laser diode was analyzed in Sec. 4.2 next. As shown in Fig. 4.11, the high-power laser diode is absolutely non-linear

*It is practical a filter 3^{rd} order, as inductance of the load's connecting wires must be considered

as a load. Accordingly, the measured and modeled transient responses of the 2^{nd*} and 3^{rd} order buck converters in Fig. 4.16 and 4.17 do not match. From my point of view, the DBR tapered laser diode is such non-linear as a buck converters load that load resistance cannot be approximated by the static resistance at the operation point. When the output voltage increases, the resistance of the high-power laser diode changes from very high to low resistance as shown in Fig. 4.11. At high load resistances, the buck converter is operating in continuous conduction mode and switches to discontinuous conduction mode at lower values. Consequently, the transient responses of a buck converter driving a high-power laser diode is hard to predict and to model. Interestingly, with a 1^{st} order buck converter, the non-linear load of the laser diode may be partially compensated by an additional inductance at some operation points and modeled with sufficient accuracy as shown in Fig. 4.18.

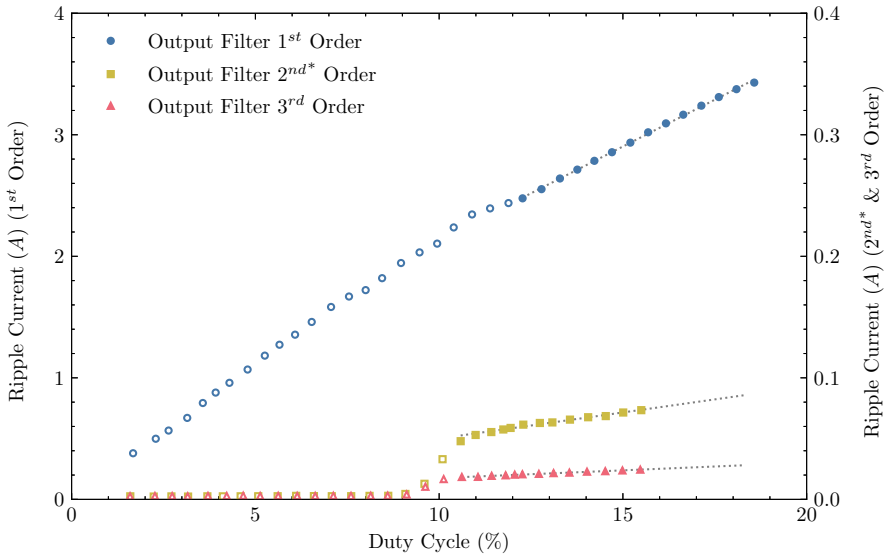

Figure 5.1.: Final comparison of the ripple amplitudes of the measured output currents: In steady-state the peak-to-peak ripple amplitudes of the output currents are measured at various duty cycles on buck converters with included wire inductance driving the DBR tapered laser diode, operating in continuous (filled markers) and discontinuous (unfilled markers) conduction mode, are compared for the output filters 1^{st}, 2^{nd*}, 3^{rd} order

Furthermore, measurements of the output current ripple were made and the filtering characteristics of the 1^{st}, 2^{nd*} and 3^{rd} order output filters of buck converters were compared. With an output filter 1^{st} order, the current ripple is mostly large and triangular as shown in Fig. 4.19. By increasing the filter to 2^{nd*} or 3^{rd} order, the current ripple becomes sinusoidal and is reduced significantly. For detailed analysis, I measured the peak-to-peak ripple amplitudes of the output currents at various duty cycles and presented them as shown in Fig. 5.1. It is a slightly modified version of Fig. 4.20. Notice, the measured amplitudes of the 1^{st} order output filter are scaled to

*It is practical a filter 3^{rd} order, as inductance of the load's connecting wires must be considered

the left and the amplitudes of the 2^{nd*} and 3^{rd} order output filters to the right axes for comparison. At duty cycles larger than 11% as shown in Fig. 5.1, the ripple amplitudes increase linearly. With lower duty cycles, the load resistance of the DBR tapered laser diode becomes high-resistance as shown in Fig. 4.11 and the buck converters operation changes from continuous to discontinuous conduction mode. Accordingly, the output current and current ripple of the 2^{nd*} and 3^{rd} order buck converter become zero. On 1^{st} order buck converter, the voltage pulses in discontinuous conduction mode are still large enough to cause a current flowing through the diode. Consequently, the amplitudes of these current pulses are measured and represented in Fig 5.1. However more interestingly, in the linear region the ripple amplitudes of the 2^{nd*} and 3^{rd} order output filters are significantly smaller than for the 1^{st} order. Moreover, the gradient of the ripple amplitudes is reduced by increasing the output inductor or equivalently the inductance of the load's connecting wires. Consequently, a buck converter 3^{rd} order is actually significantly better for filtering the output current. The research question, in which way can the buck converter be improved, is thus clearly answered.

Output Filter Order	Oscillating	Ripple Current	Controller Complexity
1^{st}	no	large	simple
2^{nd*}	yes	small	complex
3^{rd}	yes	smaller	complex

Table 5.1.: Final comparison of controller complexity versus output current filtering characteristics of 1^{st}, 2^{nd*} and 3^{rd} order buck converters

Finally, the insights obtained are contrasted once more and an outlook on the controller design complexity is given. The results are therefore briefly summarized in Tab. 5.1. It is obvious that the output current ripple is reduced with 2^{nd*} and even more with 3^{rd} order output filter. On the other hand, the output filter becomes oscillating and more complex to control. Since the high-power laser diode is such non-linear as a load, the dynamic behaviour of the buck converter is hard to model. The controller design is thus complicated and should be done experimentally. However, if the laser is operating in continuous-wave mode and the transient response is not an issue, the controller design may be done relatively simply. Additionally, in circumstances where the output current ripple is not relevant, the 1^{st} order buck converter can be easily controlled. In pulsed operation, the controller design of the 2^{nd*} and 3^{rd} order buck converters becomes much more complex, which might be overcome by special controller designs. Thus, this is still an unresolved question that could be further investigated.

*It is practical a filter 3^{rd} order, as inductance of the load's connecting wires must be considered

List of Figures

List of Tables

Bibliography

[1] A. Müller, S. Marschall, O. B. Jensen, J. Fricke, H. Wenzel, B. Sumpf, and P. E. Andersen, "Diode laser based light sources for biomedical applications", *Laser & Photonics Reviews*, vol. 7, no. 5, pp. 605–627, Sep. 2013.

[2] F. Bachmann, P. Loosen, and R. Poprawe, *High Power Diode Lasers: Technology and Applications*, 1st ed. New York, USA: Springer Science & Business Media, 2007.

[3] C. Fiebig, G. Blume, C. Kaspari, D. Feise, J. Fricke, M. Matalla, W. John, H. Wenzel, K. Paschke, and G. Erbert, "12w high-brightness single-frequency dbr tapered diode laser", *Electronics Letters*, vol. 44, no. 21, pp. 1253–1255, Oct. 2008.

[4] Z. Zeng, K. Sun, G. Wang, T. Zhang, S. Kulis, P. Gui, and P. Moreira, "A compact low-power driver array for vcsels in 65-nm cmos technology", *IEEE Transactions on Nuclear Science*, vol. 64, no. 6, pp. 1599–1604, May 2017.

[5] C. Niclass, K. Ito, M. Soga, H. Matsubara, I. Aoyagi, S. Kato, and M. Kagami, "Design and characterization of a 256x64-pixel single-photon imager in cmos for a mems-based laser scanning time-of-flight sensor", *Optics Express*, vol. 20, no. 11, pp. 11 863–11 881, May 2012.

[6] M. D. Kimbrough, "Linear laser driver circuit", U.S. Patent 6609842, Aug. 2003.

[7] M. T. Thompson and M. F. Schlecht, "High power laser diode driver based on power converter technology", *IEEE Transactions on Power Electronics*, vol. 12, no. 1, pp. 46–52, Jan. 1997.

[8] A. Sharma, C. Panwar, and R. Arya, "High power pulsed current laser diode driver", in *ICEPES International Conference on Electrical Power and Energy Systems*, Dec. 2016, pp. 120–126.

[9] Z. Yuan and H. Xu, "Pulse power supply with faster response and low ripple current using inductive storage and interleaving technology", *CPSS Transactions on Power Electronics and Applications*, vol. 5, no. 1, pp. 54–62, Apr. 2020.

[10] F.-Z. Chen, J.-Y. Wang, Y.-C. Song, and F.-S. Ho, "High efficiency synchronous pulse laser driver system", in *IEEE 3rd International Future Energy Electronics Conference and ECCE Asia*, Jun. 2017, pp. 1878–1881.

[11] R. W. Erickson and D. Maksimovic, *Fundamentals of Power Electronics*, 2nd ed. New York, USA: Springer Science & Business Media, 2001.

[12] I. Batarseh and A. Harb, "Non-isolated switch mode dc-dc converters", in *Power Electronics: Circuit Analysis and Design*, 2nd ed. Basel, CH: Springer International Publishing, 2018, pp. 173–272.

[13] R. D. Middlebrook and S. Cuk, "A general unified approach to modelling switching-converter power stages", in *IEEE Power Electronics Specialists Conference*, Jun. 1976, pp. 18–34.

[14] J. Sun, D. M. Mitchell, M. F. Greuel, P. T. Krein, and R. M. Bass, "Averaged modeling of pwm converters operating in discontinuous conduction mode", *IEEE Transactions on Power Electronics*, vol. 16, no. 4, pp. 482–492, Jul. 2001.

[15] K. Ogata, "Mathematical modeling of control systems", in *Modern control engineering*, 5th ed. Upper Saddle River, USA: Prentice Hall, 2010, pp. 13–62.

[16] G. W. Wester and R. Middlebrook, "Low-frequency characterization of switched dc-dc converters", in *IEEE Power Processing and Electronics Specialists Conference*, May 1972, pp. 9–20.

[17] T. Suntio, "Unified average and small-signal modeling of direct-on-time control", *IEEE Transactions on Industrial Electronics*, vol. 53, no. 1, pp. 287–295, Feb. 2006.

[18] T. Suntio, "Average and small-signal modeling of direct-on-time controlled converters", in *Dynamic Profile of Switched-Mode Converter: Modeling, Analysis and Control*, 1st ed. Weinheim, DE: Wiley-VCH Verlag, 2009, pp. 59–120.

[19] C. K. Alexander, "Two-port networks", in *Fundamentals of Electric Circuits*, 4th ed. New York, USA: McGraw-Hill, 2009, pp. 849–901.

[20] M. Hankaniemi and T. Suntio, "Small-signal models for constant-current regulated converters", in *32nd Annual Conference on IEEE Industrial Electronics*, Nov. 2006, pp. 2037–2042.

[21] W. A. Martin and R. J. Fateman, "The macsyma system", in *SYMSAC Proceedings of the second ACM symposium on Symbolic and algebraic manipulation*, Mar. 1971, pp. 59–75.

[22] A. Lidow, "Gallium nitride integration: Breaking down technical barriers quickly [expert view]", *IEEE Power Electronics Magazine*, vol. 7, no. 1, pp. 56–63, Feb. 2020.

[23] A. Lidow, M. De Rooij, J. Strydom, D. Reusch, and J. Glaser, *GaN Transistors for Efficient Power Conversion*, 3rd ed. Hoboken, USA: John Wiley & Sons, 2019.

[24] R. W. Erickson, "Optimal single resistors damping of input filters", in *14th Annual Applied Power Electronics Conference and Exposition*, Mar. 1999, pp. 1073–1079.

[25] L. W. Nagel and D. Pederson, "Spice (simulation program with integrated circuit emphasis)", EECS Department, University of California, Berkeley, Tech. Rep. UCB/ERL M382, Apr. 1973.

[26] S. Lahti, P. Sjövall, J. Vanne, and T. D. Hämäläinen, "Are we there yet? a study on the state of high-level synthesis", *IEEE Transactions on Computer-Aided Design of Integrated Circuits and Systems*, vol. 38, no. 5, pp. 898–911, May 2018.

[27] T. E. Oliphant, "Python for scientific computing", *Computing in Science & Engineering*, vol. 9, no. 3, pp. 10–20, Jun. 2007.

Appendix A.

Dynamic Modeling of a Buck Converter

A.1. Kirchhoff's voltage and current laws in different modes of operation

The Kirchhoff's voltage and current laws in Mode 1 for time t_{on} in CCM are given in Eq. (A.1) to (A.4), which are derived from the simplified schematics in Fig. 2.9.

$$u_{L_{(on)}} = u_{in} - u_o - (r_{ds1} + r_L) i_{L_{(on)}} \quad \text{(A.1)} \qquad i_{C_{(on)}} = i_{L_{(on)}} - i_o \quad \text{(A.2)}$$

$$i_{in_{(on)}} = i_{L_{(on)}} \quad \text{(A.3)} \qquad u_{o_{(on)}} = u_{C_{(on)}} + r_C \, i_{C_{(on)}} \quad \text{(A.4)}$$

Kirchhoff's voltage and current laws in Mode 2 for time t_{off} in CCM (derived from Fig. 2.10).

$$u_{L_{(off)}} = -u_o - (r_{ds1} + r_L) i_{L_{(off)}} \quad \text{(A.5)} \qquad i_{C_{(off)}} = i_{L_{(off)}} - i_o \quad \text{(A.6)}$$

$$i_{in_{(off)}} = 0 \quad \text{(A.7)} \qquad u_{o_{(off)}} = u_{C_{(off)}} + r_C \, i_{C_{(off)}} \quad \text{(A.8)}$$

Kirchhoff's voltage and current laws in Mode 2 for time t_{off_1} in DCM (derived from Fig. 2.12).

$$u_{L_{(off1)}} = -u_o - U_D - (r_D + r_L) i_{L_{(off1)}} \quad \text{(A.9)} \qquad i_{C_{(off1)}} = i_{L_{(off1)}} - i_o \quad \text{(A.10)}$$

$$u_{o_{(off1)}} = u_{C_{(off1)}} + r_C \, i_{C_{(off1)}} \quad \text{(A.11)} \qquad i_{in_{(off1)}} = 0 \quad \text{(A.12)}$$

A.2. Conversion of Two Port Networks

The two-port network theory [19] is handy for analyzing complex circuits. In this theory, the different parameter representations in matrix form have several properties, which are highly beneficial. Consequently, they are helpful to convert two-port networks into other parameter representations.

The modeling results of the buck converters operating in continuous or discontinuous conduction mode are typically given in g-parameter matrix form as shown in Eq. (A.13). By analyzing the matrix elements separately some interesting correlations of the input and output ports are found in Eq. (A.14) to (A.19). They are calculated from Eq. (A.13) by basic mathematical manipulations.

$$\begin{bmatrix} \hat{i}_{in} \\ \\ \hat{u}_o \end{bmatrix} = \begin{bmatrix} g_{11} & g_{12} & g_{13} \\ \\ g_{21} & g_{22} & g_{23} \end{bmatrix} \begin{bmatrix} \hat{u}_{in} \\ \hat{i}_o \\ \hat{d} \end{bmatrix} \tag{A.13}$$

$$g_{11} = \left.\frac{\hat{i}_{in}}{\hat{u}_{in}}\right|_{\hat{i}_o=\hat{d}=0} \quad \text{(A.14)} \qquad g_{12} = \left.\frac{\hat{i}_{in}}{\hat{i}_o}\right|_{\hat{u}_{in}=\hat{d}=0} \quad \text{(A.15)} \qquad g_{13} = \left.\frac{\hat{i}_{in}}{\hat{d}}\right|_{\hat{u}_{in}=\hat{i}_o=0} \quad \text{(A.16)}$$

$$g_{21} = \left.\frac{\hat{u}_o}{\hat{u}_{in}}\right|_{\hat{i}_o=\hat{d}=0} \quad \text{(A.17)} \qquad g_{22} = \left.\frac{\hat{u}_o}{\hat{i}_o}\right|_{\hat{u}_{in}=\hat{d}=0} \quad \text{(A.18)} \qquad g_{23} = \left.\frac{\hat{u}_o}{\hat{d}}\right|_{\hat{u}_{in}=\hat{i}_o=0} \quad \text{(A.19)}$$

To convert the g-parameter form to the a-parameters representation, Eq. (A.13) is split up in two equations, which are rearranged and represented in a-parameter matrix form in Eq. (A.20). Thus, the g-parameters can be converted easily to the a-parameter representation. In Eq. (A.21) the general a-parameter matrix representation is shown. A special property of the a-parameter matrix is that two cascaded matrices can be combined by a matrix multiplication.

$$\begin{bmatrix} \hat{u}_{in} \\ \\ \hat{i}_{in} \end{bmatrix} = \frac{1}{g_{21}} \begin{bmatrix} 1 & -g_{22} & -g_{23} \\ \\ g_{11} & g_{12}g_{21} - g_{11}g_{22} & g_{13}g_{21} - g_{11}g_{23} \end{bmatrix} \begin{bmatrix} \hat{u}_o \\ \hat{i}_o \\ \hat{d} \end{bmatrix} \tag{A.20}$$

$$\begin{bmatrix} \hat{u}_{in} \\ \\ \hat{i}_{in} \end{bmatrix} = \begin{bmatrix} a_{11} & a_{12} & a_{13} \\ \\ a_{21} & a_{22} & a_{23} \end{bmatrix} \begin{bmatrix} \hat{u}_o \\ \hat{i}_o \\ \hat{d} \end{bmatrix} \tag{A.21}$$

$$a_{11} = \left.\frac{\hat{u}_{in}}{\hat{u}_o}\right|_{\hat{i}_o=\hat{d}=0} \quad (A.22) \qquad a_{12} = \left.\frac{\hat{u}_{in}}{\hat{i}_o}\right|_{\hat{u}_o=\hat{d}=0} \quad (A.23) \qquad a_{13} = \left.\frac{\hat{u}_{in}}{\hat{d}}\right|_{\hat{u}_o=\hat{i}_o=0} \quad (A.24)$$

$$a_{21} = \left.\frac{\hat{i}_{in}}{\hat{u}_o}\right|_{\hat{i}_o=\hat{d}=0} \quad (A.25) \qquad a_{22} = \left.\frac{\hat{i}_{in}}{\hat{i}_o}\right|_{\hat{u}_o=\hat{d}=0} \quad (A.26) \qquad a_{23} = \left.\frac{\hat{i}_{in}}{\hat{d}}\right|_{\hat{u}_o=\hat{i}_o=0} \quad (A.27)$$

In order to determine the voltage controlled buck converter transfer functions, the g-parameter matrix of the entire circuit is needed. Therefore, it is convenient to convert the a-parameter matrix to the g-parameter form in Eq. (A.13). The conversion is done by Eq. (A.28).

$$\begin{bmatrix} \hat{i}_{in} \\ \\ \hat{u}_o \end{bmatrix} = \frac{1}{a_{11}} \begin{bmatrix} a_{21} & a_{11}a_{22} - a_{12}a_{21} & a_{11}a_{23} - a_{13}a_{21} \\ \\ 1 & -a_{12} & -a_{13} \end{bmatrix} \begin{bmatrix} \hat{u}_{in} \\ \hat{i}_o \\ \hat{d} \end{bmatrix} \quad (A.28)$$

For determining the current controlled buck converter transfer functions, the y-parameter representation is more useful. Correspondingly, the a-parameter matrix should be converted to the y-parameter form, which is done with Eq. (A.29). The general form of the y-parameter matrix is given in Eq. (A.30) and the following parameters are derived.

$$\begin{bmatrix} \hat{i}_{in} \\ \\ \hat{i}_o \end{bmatrix} = \frac{1}{a_{12}} \begin{bmatrix} a_{22} & a_{12}a_{21} - a_{11}a_{22} & a_{12}a_{23} - a_{13}a_{22} \\ \\ 1 & -a_{11} & -a_{13} \end{bmatrix} \begin{bmatrix} \hat{u}_{in} \\ \hat{u}_o \\ \hat{d} \end{bmatrix} \quad (A.29)$$

$$\begin{bmatrix} \hat{i}_{in} \\ \\ \hat{i}_o \end{bmatrix} = \begin{bmatrix} y_{11} & y_{12} & y_{13} \\ \\ y_{21} & y_{22} & y_{23} \end{bmatrix} \begin{bmatrix} \hat{u}_{in} \\ \hat{u}_o \\ \hat{d} \end{bmatrix} \quad (A.30)$$

$$y_{11} = \left.\frac{\hat{i}_{in}}{\hat{u}_{in}}\right|_{\hat{u}_o=\hat{d}=0} \quad (A.31) \qquad y_{12} = \left.\frac{\hat{i}_{in}}{\hat{u}_o}\right|_{\hat{u}_{in}=\hat{d}=0} \quad (A.32) \qquad y_{13} = \left.\frac{\hat{i}_{in}}{\hat{d}}\right|_{\hat{u}_{in}=\hat{u}_o=0} \quad (A.33)$$

$$y_{21} = \left.\frac{\hat{i}_o}{\hat{u}_{in}}\right|_{\hat{u}_o=\hat{d}=0} \quad (A.34) \qquad y_{22} = \left.\frac{\hat{i}_o}{\hat{u}_o}\right|_{\hat{u}_{in}=\hat{d}=0} \quad (A.35) \qquad y_{23} = \left.\frac{\hat{i}_o}{\hat{d}}\right|_{\hat{u}_{in}=\hat{u}_o=0} \quad (A.36)$$

Appendix B.

Measurements and Verification

Measuring Instrument	Data Source
Power Supply GW Instek GPS-4303	https://www.gwinstek.com/en-global/products/detail/GPS-x303
Oscilloscope LeCroy WaveRunner 104MXi	https://cdn.teledynelecroy.com/files/manuals/wrxi_om_revc.pdf
Current Probe LeCroy AP015	https://cdn.teledynelecroy.com/files/manuals/ap015_current_probe_manual.pdf
Thermal Camera Fluke Ti25	https://dam-assets.fluke.com/s3fs-public/ti10____umeng0200.pdf

Table B.1.: List of measuring instruments

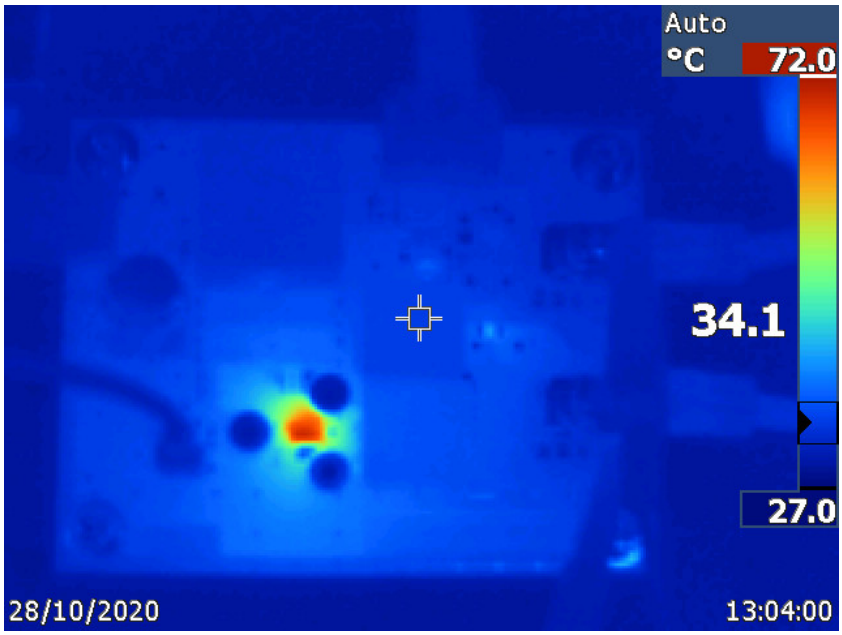

Figure B.1.: Thermal image of the implemented buck converter: The image was taken from the 3^{rd} order buck converter driving a continuous current of $10.3A$ at 18.3% duty cycle into the tapered section of a DBR tapered laser diode without an heatsink at an ambient temperature of $25°C$